Ocean Engineering 116 (2016) 295–311

Contents lists available at ScienceDirect

Ocean Engineering

journal homepage: www.elsevier.com/locate/oceaneng

The effects of wave activity on overtopping and scouring on a vertical breakwater

N. Tofany [a,*], M.F. Ahmad [b], M. Mamat [c], H. Mohd-Lokman [a]

[a] School of Marine Science and Environment, Universiti Malaysia Terengganu, Malaysia
[b] School of Ocean Engineering, Universiti Malaysia Terengganu, Malaysia
[c] Faculty of Informatics and Computing, Universiti Sultan Zainal Abidin, Malaysia

ARTICLE INFO

Article history:
Received 13 November 2014
Accepted 2 March 2016
Available online 17 March 2016

Keywords:
The RANS-VOF model
Hydrodynamics
Sediment transport
Scour
Breakwater
Overtopping discharge

ABSTRACT

A numerical study is presented herein to investigate the effects of wave activity on overtopping discharges and scouring offshore of a vertical breakwater. A 2D RANS-VOF model was used to study this topic. The model was coupled with turbulence closure, sediment transport, and morphological models with additional bottom shear stresses in the momentum equations. Validation results show that the numerical predictions of velocities are in good agreement with the experimental data and the analytical solution. The predicted scour patterns and maximum equilibrium scour depths also show better accuracy than the results of existing models. Numerical experiments were then conducted by varying wave and breakwater height (freeboard) which result in different overtopping discharges. The effects of different wave heights and freeboards on the overtopping discharge, and the subsequent effects on the hydrodynamics and scouring were analyzed. The results of this analysis will be discussed in details in this paper and are expected to be worthwhile in the process of designing breakwater in coastal areas.

1. Introduction

Complex interactions between waves and a breakwater generate phenomenon that may induce undesired scour offshore of the breakwater. The inducing phenomenon are such as standing waves, vortices, wave reflections, breaking waves, turbulence flow, etc. A substantial scour hole at the toe of a breakwater (toe scouring) can damage its structure and thus threatens the safety of the protected areas behind it. Nine research institutions from six European countries, even considered the serious threat of scour through extensive field and laboratory studies under the project of Scour Around Coastal Structures (SCARCOST). The results are summarized by Sumer et al. (2001). Another study by the US Army Corps of Engineers (Lillycrop and Hughes, 1993) also reported various failure mechanisms of breakwaters due to scour. The results can be reviewed in the paper of Oumeraci (1994). Therefore, understanding the formation of scour and the inducing mechanisms is highly important research topic.

Standing waves are one of the main inducing mechanisms for the toe scouring formed offshore of vertical breakwaters. Müller et al. (2008) reported that toe scouring is attributed to wave reflections which increase wave heights (through the formation of standing waves), velocities and turbulence. Depending on the reflected wave characteristics, standing waves may vary from fully or partially as studied by Young and Testik (2011). In addition to the toe scouring, Allsop et al. (2005) and Müller et al. (2008) reported that wave overtopping is the critical response of vertical breakwaters. Yeganeh-Bakhtiary et al. (2010) and Tahersima et al. (2011) showed that wave overtopping is significant in changing the characteristics of reflected waves and scour patterns offshore of the breakwater. In other studies (Xie, 1981; Lee and Mizutani, 2008), wave conditions and breakwater height have been reported as the important factors on the hydrodynamics and scour patterns generated offshore of vertical breakwaters. These findings lead to a question of what will happen on the hydrodynamics and scour patterns offshore of the vertical breakwaters if these two factors are considered as the factors that influence the rate of overtopping discharge. The present study is conducted to investigate this issue.

A number of researchers had conducted the experimental works of scouring around the breakwaters. The problem of scour offshore of a vertical breakwater was early studied by de Best and Bijker (1971) and Xie (1981). They found that scour patterns were different for fine and coarse materials. Xie (1981) proposed two basic scour patterns. The patterns are now widely used as the reference patterns for studying scour offshore of a vertical breakwater. The other experimental studies are such as Irie and

* Correspondence to: School of Marine Science and Environment, Universiti Malaysia Terengganu, 21030 Kuala Terengganu, Terengganu, Malaysia. Tel.: +60 9 6683236.
E-mail addresses: novan.tofany@umt.edu.my, novtov354@gmail.com (N. Tofany).

http://dx.doi.org/10.1016/j.oceaneng.2016.03.007
0029-8018/

Nadaoka (1984), Hughes and Fowler (1991) for vertical breakwaters, Sumer and Fredsøe (2000) for rubble mound breakwaters, Sumer et al. (2005) for submerged sloped breakwaters, and Lee and Mizutani (2008) for vertical submerged breakwaters. These studies also showed that the re-circulating cells of steady streaming formed under standing waves have significant effects on the formation of scour. The effects of overtopping on the hydrodynamics of standing waves were specifically studied by Zhang et al. (2001). They measured the maximum horizontal velocity of water particles near the node of standing waves offshore of a vertical breakwater. It was shown that overtopping decreased the maximum horizontal velocity of fluid particles.

Numerical studies investigating scour under the influence of overtopping are relatively rare. Notable studies include Yeganeh-Bakhtiary et al. (2010) and Tahersima et al. (2011) that numerically studied the overtopping effects on the hydrodynamics of standing waves and scour offshore of vertical breakwaters. Yeganeh-Bakhtiary et al. (2010) studied the hydrodynamics aspects using a model based on the Reynolds Averaged Navier Stokes (RANS) equations and Volume of Fluid (VOF) method. Tahersima et al. (2011) coupled the model with the sediment transport formulae of Engelund-Fredsøe (1976) and Bijker (1971) and a morphological model of Fredsøe and Deigaard (1992) to simulate the scouring process, although limitations were evident in the scour simulations when compared to the result of Xie (1981). Gislason et al. (2009a,b) used the same sediment transport models as used by Tahersima et al. (2011) which coupled with a 3D Navier–Stokes solver and a k–ω turbulence model. Their simulated scour pattern was in good agreement with the experimental data of Sumer et al. (2005) for the vertical breakwater case, yet it was not accurate in the sloped breakwater case. Hajivalie et al. (2012) applied an Euler–Lagrange modeling approach for the simulation of scour offshore of a vertical breakwater. Although their simulated scour patterns could resemble the pattern of Xie (1981), however, the effects of overtopping were beyond the scope of their study. In addition, none of these studies have ever investigated the effects of different overtopping discharges. This unexplored issue and the lacks of existing numerical results have produced a gap of knowledge on the hydrodynamics and scour offshore of vertical breakwaters. The present study is therefore conducted to bridge this gap.

In the present work, the two-dimensional numerical model of Tofany et al. (2014) is applied to study the effects of different overtopping discharges on the hydrodynamics and scour patterns offshore of vertical breakwaters. The model combines the hydrodynamic model, consisting of the RANS equations, VOF method, and a k–ε turbulence model, with the sediment transport formula of Bailard (1981) and the morphological model of Fredsøe and Deigaard (1992). Additional terms of bottom shear stress as used by Karambas (1998) are added into the momentum equations. There has not been any study that ever used this modeling approach to the present simulation problem.

Tofany et al. (2014) have shown that the numerical results of this model were encouraging. The computed near bottom velocities were found in close agreements with the experimental data and analytical solution. Although the model did not simulate the scour/deposition pattern in the equilibrium state, the simulated patterns showed better agreement with the patterns as found in the experimental results of Xie (1981) and Sumer et al. (2005) than the numerical results of Tahersima et al. (2011) and Gislason et al. (2009b). It was also interesting to find that the additional terms of bottom shear stress were significant to produce physical scour patterns, because without these terms in the model, the physical scour patterns could not be obtained. The model was also successfully applied to extend the knowledge of breakwater steepness effects on the hydrodynamics and scouring offshore of sloped impermeable breakwaters (Tofany et al., 2014).

In this study, two numerical experiments were conducted to investigate the effects of wave overtopping and different overtopping discharges due to different wave conditions and breakwater heights (freeboards). Validation results of the model for fluid velocities and equilibrium scour patterns are presented earlier. The results of the numerical experiments showed that overtopping reduces the energy of the reflected waves. Consequently, the intensity of re-circulating cells offshore of the breakwater is decreased and thus reduces the sizes of scour depths/deposition ridges. It even prevents the toe scouring to develop offshore of the breakwater, in which the scour at this area can affect the breakwater stability. It was also found that wave characteristics, intensity of the re-circulating cells, and sizes of the scour depths/deposition ridges are highly affected by the rate of overtopping discharge. The detailed discussion will be presented in this paper.

2. The numerical model

Tofany et al. (2014) developed the 2D RANS-VOF model by modifying the SOLA-VOF code. The SOLA-VOF code is a solution algorithm for various cases of transient fluid flows involving free surface motions. The code provides important components required for the present simulation such as the two-dimensional incompressible Navier–Stokes equations for describing the flow field, the Volume of Fluid (VOF) method for tracking free surface motions, and other features that can be seen more detail in Nichols et al. (1980). Some modifications were made to the original code to make it more suitable for simulating the wave–structure–sediment interactions. The following describes the main components of the present model after modifying the original code.

2.1. Governing equations

The governing equations of fluid flow are the RANS equations and the k–ε turbulence closure model. The additional bottom shear stresses of Karambas (1998) are included in the momentum equations using. In a two-dimensional domain, the equations are given as follows:

$$\frac{\partial \theta u}{\partial x}+\frac{\partial \theta v}{\partial y}=0, \tag{1}$$

$$\frac{\partial \theta u}{\partial t}+\theta u\frac{\partial \theta u}{\partial x}+\theta v\frac{\partial \theta u}{\partial y}=\theta\frac{\partial}{\partial x}\left[2(\upsilon+\upsilon_t)\frac{\partial \theta u}{\partial x}\right]+\theta\frac{\partial}{\partial y}\left[(\upsilon+\upsilon_t)\left(\frac{\partial \theta u}{\partial y}+\frac{\partial \theta v}{\partial x}\right)\right] -\frac{\theta}{\rho}\frac{\partial p}{\partial x}-\frac{\tau_{bx}}{\rho}, \tag{2}$$

$$\frac{\partial \theta v}{\partial t}+\theta u\frac{\partial \theta v}{\partial x}+\theta v\frac{\partial \theta v}{\partial y}=\theta\frac{\partial}{\partial y}\left[2(\upsilon+\upsilon_t)\frac{\partial \theta v}{\partial y}\right]+\theta\frac{\partial}{\partial x}\left[(\upsilon+\upsilon_t)\left(\frac{\partial \theta v}{\partial x}+\frac{\partial \theta u}{\partial y}\right)\right] -\frac{\theta}{\rho}\frac{\partial p}{\partial y}-g-\frac{\tau_{by}}{\rho}, \tag{3}$$

$$\frac{\partial \theta k}{\partial t}+\theta u\frac{\partial \theta k}{\partial x}+\theta v\frac{\partial \theta k}{\partial y}=\frac{\partial}{\partial x}\left[\left(\upsilon+\frac{\upsilon_t}{\sigma_k}\right)\frac{\partial \theta k}{\partial x}\right]+\frac{\partial}{\partial y}\left[\left(\upsilon+\frac{\upsilon_t}{\sigma_k}\right)\frac{\partial \theta k}{\partial y}\right]P_r-\varepsilon, \tag{4}$$

$$\frac{\partial \theta \varepsilon}{\partial t}+\theta u\frac{\partial \theta \varepsilon}{\partial x}+\theta v\frac{\partial \theta \varepsilon}{\partial y}=\frac{\partial}{\partial x}\left[\left(\upsilon+\frac{\upsilon_t}{\sigma_\varepsilon}\right)\frac{\partial \theta \varepsilon}{2\partial x}\right]+\frac{\partial}{\partial y}\left[\left(\upsilon+\frac{\upsilon_t}{\sigma_\varepsilon}\right)\frac{\partial \theta \varepsilon}{\partial y}\right] +C_{\varepsilon 1}(P_r)\frac{\varepsilon}{k}-C_{\varepsilon 2}\varepsilon\frac{\varepsilon}{k}, \tag{5}$$

$$P_r=\upsilon_t\left[2\left(\frac{\partial \theta u}{\partial x}\right)^2+2\left(\frac{\partial \theta v}{\partial y}\right)^2+\left(\frac{\partial \theta u}{\partial y}+\frac{\partial \theta v}{\partial x}\right)^2\right], \tag{6}$$

Table 1
Constants of the k–ε turbulence closure model (Launder and Spalding, 1974).

Parameter	C_d	$C_{\varepsilon 1}$	$C_{\varepsilon 2}$	σ_k	σ_ε
Value	0.09	1.44	1.92	1.00	1.30

$$\upsilon_t = C_d \frac{k^2}{\varepsilon}, \tag{7}$$

where t is time, u and v are the mean velocity components in x and y direction respectively, p is the mean pressure, and g is the vertical gravity acceleration, ρ is the fluid density, υ and υ_t are respectively the fluid and eddy viscosities, k is the turbulence kinetic energy, P_r is the production of turbulence kinetic energy, ε is the turbulence dissipation rate, θ is the partial cell treatment parameters, τ_{bx} and τ_{by} are the bottom shear stresses. The model constants are set following to Launder and Spalding (1974) (see Table 1). The bottom shear stresses are estimated from Karambas (1998):

$$\frac{\tau_{bx}}{\rho} = \frac{f_w}{2} u_b \sqrt{u_b^2 + v_b^2}, \tag{8a}$$

$$\frac{\tau_{by}}{\rho} = \frac{f_w}{2} v_b \sqrt{u_b^2 + v_b^2}, \tag{8b}$$

where u_b and v_b are the horizontal and vertical components of the near bottom velocity, and f_w is the friction coefficient.

2.2. Boundary conditions

The present model uses the Volume of Fluid (VOF) method (Hirt and Nichols, 1981) to track the free surface motion by solving the volume of fluid function, F, in the following transport equation:

$$\frac{\partial \theta F}{\partial t} + \theta u \frac{\partial F}{\partial x} + \theta v \frac{\partial F}{\partial y} = 0, \tag{9}$$

At the inflow boundary, the Dirichlet- type wave generator and the weakly reflecting boundary (Petit et al., 1994) are applied as follows:

$$\frac{\partial \varphi}{\partial t} - C\frac{\partial \varphi}{\partial x} = \frac{\partial \varphi_i}{\partial t} - C\frac{\partial \varphi_i}{\partial x}, \tag{10}$$

where φ_i is the variable of incident wave signals and φ is for the computed variables, including the free surface displacement and velocities. The weakly reflecting boundary is applied at the inflow boundary to reduce the effect of intermixing between the generated incident waves and unphysical reflected waves at the inflow. It is also applied at the outflow boundary for overtopping cases to let the fluid passes through the open boundary completely. The partial cell treatment technique of the NASA-VOF2D code (Torrey et al., 1985) is adapted to create the breakwater that is placed at the outflow of the domain. No-slip rigid wall is taken as the boundary conditions at the bottom and along the solid boundary of the breakwater structure.

An assumption for zero vertical fluxes of k and ε is taken as the turbulence boundary conditions at the free surface:

$$\frac{\partial k}{\partial n} = 0, \frac{\partial \varepsilon}{\partial n} = 0, \tag{11}$$

The Neumann continuative boundary condition is defined at the inflow of turbulence boundary:

$$\left(\frac{\partial k}{\partial x}\right)_{x=0} = 0, \left(\frac{\partial \varepsilon}{\partial x}\right)_{x=0} = 0, \tag{12}$$

and no-slip rigid wall without turbulent boundary layer is assumed at the bottom and along the solid boundaries. Fig. 1 describes the setup of computational domain and boundary conditions applied in the simulation.

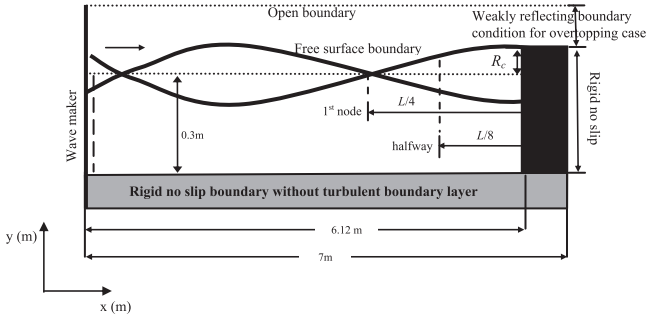

Fig. 1. Setup of computational domain and the standing wave description. L is the wavelength and R_c is freeboard.

2.3. Initial conditions

All simulations are initialized with zero velocity and hydrostatic pressure for fluid field, and flat bed profile is initialized at $y=0$ m at the bottom. The initial conditions for the turbulence field are set according to Lin and Liu (1998) and Bakhtyar et al. (2009) as follows:

$$k = \frac{1}{2} u_t^2, u_t = \delta C, \delta = 0.0025, \tag{13}$$

$$\varepsilon = C_d \frac{k^2}{\upsilon_t}, \upsilon_t = \epsilon \upsilon, \epsilon = 0.1, \tag{14}$$

where C is the wave celerity at the inflow boundary, C_d is the empirical coefficient as given in Table 1.

2.4. Cross-shore sediment transport model

For sediment transport calculation, the formula of Bailard (1981) is used with an assumption of non-cohesive sediment. The total volumetric sediment transport rate, $S_T(t)$, is formulated as below:

$$S_T(t) = S_b(t) + S_s(t), \tag{15}$$

$$S_b(t) = \frac{\rho c_f \epsilon_b}{(\rho_s - \rho) g (1-p) \tan\varphi} \left\{ \langle |u_b(t)|^2 u_b(t) \rangle - \frac{\tan\alpha}{\tan\varphi} \langle |u_b(t)|^3 \rangle \right\}, \tag{16}$$

$$S_s(t) = \frac{\rho c_f \epsilon_s}{(\rho_s - \rho) g (1-p) w} \left\{ \langle |u_b(t)|^3 u_b(t) \rangle - \frac{\epsilon_s}{w} \tan\alpha \langle |u_b(t)|^5 \rangle \right\}, \tag{17}$$

here, $S_b(t)$ and $S_s(t)$ are the volumetric sediment transport rates for bed-load and suspended-load, respectively; g is the gravity acceleration, ρ is the density of fluid, ρ_s is the density of sediment, w is the fall velocity of sediment, ε_b and ε_s are the bed-load and suspended-load efficiency factors, respectively, c_f is the drag coefficient of the bed, p is the sediment porosity, φ is the angle of repose, α is the bed-slope angle, $u_b(t)$ is the instantaneous near bottom fluid velocity, and $\langle\ \rangle$ is for time-average; Table 6 presents the parameters used in the current simulation. In the Bailard's original equation, it is recommended to use the value of $c_f = 0.005$ (Changkuan, 1994). Meanwhile, in the present work, $c_f = 0.5 f_w$ is used following the recommendations from the existing literatures (Soulsby, 1997; Changkuan, 1994; Lakhan, 2003; Reeve et al., 2004), in which the skin friction factor, f_w, is formulated based on Jonsson (1966) as follows:

$$f_w = exp\left(5.213\left(\frac{a_o}{r}\right)^{-0.194} - 5.977\right), \ for \frac{a_o}{r} \geq 1.59, \tag{18a}$$

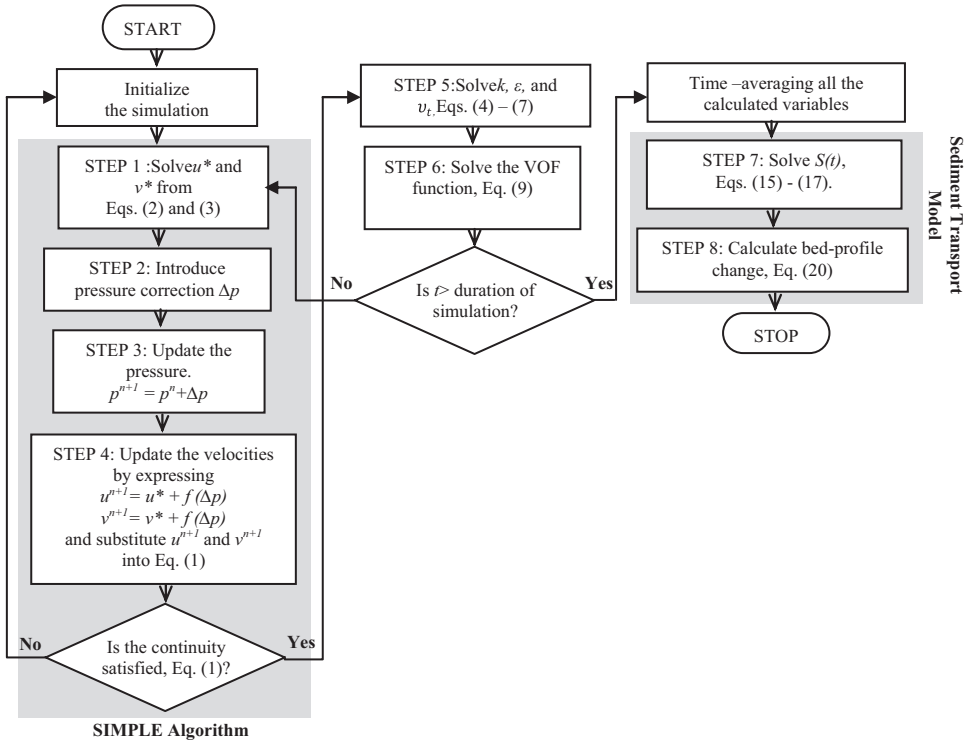

Fig. 2. Flow chart of numerical algorithm.

$$f_w = 0.3, \quad for \frac{a_o}{r} < 1.59, \tag{18b}$$

where r is the bed roughness that assumed as equal to D_{50}, and a_o is the amplitude of orbital motion at the bottom, for the first order linear wave theory:

$$a_o = \frac{H}{2\sinh\left(\frac{2\pi d}{L}\right)} \tag{19}$$

where d is the water depth. The change of bed profile is calculated using the Exner equation as described in the book of Leliavsky (1955). This equation states that the change in bed elevation, η, over time, t, is equal to one over the grain packing density, ε_o, times the negative divergence of sediment flux, S_T. The Exner equation is used in its one-dimensional form as follows:

$$\frac{\partial \eta}{\partial t} = -\frac{1}{\epsilon_o}\frac{\partial S_T}{\partial x} \tag{20}$$

where $\varepsilon_o = (1-p)$ with p is the porosity of sediment and x is downstream distance.

2.5. Numerical solutions

The six unknown variables in Eqs. (1)–(7) and (9), u, v, p, F, k, and ε were solved using the finite difference method in a staggered grid. The solution algorithm for the RANS equations was the Simple Implicit Method for Pressure-Linked Equations (SIMPLE) algorithm, firstly proposed by Patankar (1980). The VOF equation was solved using the donor–acceptor algorithm (Hirt and Nichols, 1981). Fig. 2 shows the flow chart of the algorithm utilized in the present study. In every time cycle, the size of time-step was adjusted to fulfill the following stability criteria taken from Bakhtyar et al. (2009):

- The fluid cannot travel more than one computational cell in each time-step:

$$\Delta t \le \min\left(0.3\frac{\Delta x}{|u|}, 0.3\frac{\Delta y}{|v|}\right), \tag{21}$$

- Momentum must not diffuse more than approximately one cell in one time-step:

$$\Delta t \le \min\left(\frac{1}{2(\upsilon+\upsilon_t)}\frac{\Delta x^2 \Delta y^2}{(\Delta x^2+\Delta y^2)}\right), \tag{22}$$

- Surface waves cannot travel more than one cell in each time-step:

$$\Delta t \le \min\left(\frac{\Delta x}{\sqrt{gd}}\right), \tag{23}$$

- The relative variations of k and ε in a time step should be significantly less than unity:

$$\Delta t \le \min\left(\frac{k}{\epsilon}\right) \text{ and} \Delta t \le \min\left(\frac{1}{C_{\epsilon 2}}\frac{k}{\epsilon}\right), \tag{24}$$

3. Model validation

This chapter presents validation results of the present model. The validated data are fluid velocities and scour/deposition patterns. Section 3.1 below presents the validation results of fluid velocities while Section 3.2 presents the validation results of scour/deposition patterns.

3.1. Validation of fluid velocities

Validation of the present model in predicting fluid velocities was performed using two different velocity data. They are the horizontal orbital velocity (u) field patterns, and the maximum horizontal velocity at the bottom (u_b). Table 2 presents the simulation conditions and Fig. 3 illustrates the numerical domains used for these validations, which resemble the experimental setup of Xie (1981) and Zhang et al. (2001). For the first data type, the model results were compared with the experimental data of Xie (1981) in simulating Tests 1, 2, and 3 of Table 2. For the second data type, the model results were compared with the experimental data of Xie (1981) and Zhang et al. (2001) in simulating all tests in Table 2 and also compared with the second order theory of standing waves (Miche, 1944).

However, prior to the velocities validations, a grid convergence test was performed to choose the best grid size. The grid convergence test simulated Test 2 in Table 2 for 10T long duration using nine different grid sizes. The simulated data were the horizontal components of orbital velocity field patterns. Accuracies of the nine grid sizes in terms of the averaged percentage errors and their computational times were analyzed and compared to each other; the results are presented in Table 3. The percentage errors were calculated from $\left|\frac{u_e-u_n}{u_e}\right| \times 100\%$ at each measurement point, where u_e and u_n are the experimental and numerical values, respectively. The percentage errors of the three measurement points either under the node or halfway of the standing waves were then averaged to obtain the results presented in columns 5 and 6 of Table 3. The values in columns 5 and 6 were then averaged again to obtain the error values in column 7 of Table 3.

Grid 4 was decided as the grid size for all validation and simulation cases in this study instead of Grid 6 and Grid 8 which have smaller errors. The following considerations underlie this choice. Firstly, the errors under the locations of node and halfway of Grid 4 are more proportional than the errors of Grid 6. Accuracy at the halfway is even better than the accuracy of Grid 6. Secondly, Grid 4 is more computationally efficient. The computational times

Table 2
Simulation conditions for the validation of velocities.

Experiment	Flume	Test	d (m)	H_i (m)	T (s)	L (m)	d/L	H/L	h_{wall}	Overtop
Xie (1981)	Small	1	0.30	0.050	2.41	4.00	0.075	0.013	1.00	No
		2	0.30	0.065	1.53	2.40	0.125	0.027	1.00	No
		3	0.30	0.057	1.86	3.00	0.100	0.019	1.00	No
		4	0.30	0.06	3.56	6.00	0.050	0.010	1.00	No
		5	0.30	0.050	1.17	1.71	0.175	0.029	1.00	No
		6	0.30	0.057	1.32	2.00	0.150	0.029	1.00	No
	Large	7	0.50	0.050	1.70	3.33	0.150	0.015	1.20	No
		8	0.50	0.075	3.12	6.67	0.075	0.011	1.20	No
		9	0.50	0.100	3.12	6.67	0.075	0.015	1.20	No
		10	0.50	0.060	1.70	3.33	0.150	0.018	1.20	No
Zhang et al. (2001)		11	0.65	0.090	1.40	2.70	0.241	0.033	0.75	No
		12	0.65	0.120	1.40	2.70	0.241	0.044	0.75	Yes
		13	0.65	0.150	1.40	2.70	0.241	0.056	0.75	Yes
		14	0.65	0.180	1.40	2.70	0.241	0.067	0.75	Yes

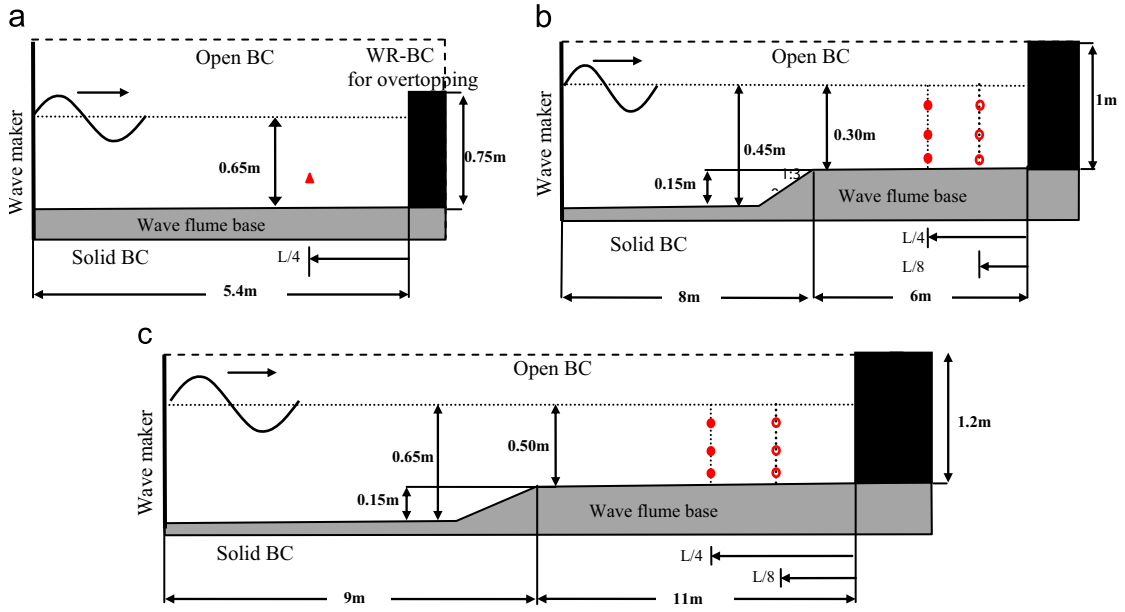

Fig. 3. Three wave flumes for the validation of fluid velocities. (a) The flume of Zhang et al. (2001), (b) the small flume and(c)the large flume of Xie (1981). *Note*: BC = Boundary Conditions. WR-BC = Weakly Reflecting Boundary Conditions. Measurement points of Xie (1981) = ● (under the 1st node, $L/4$) and ○ (under the halfway, $L/8$). The depths of measurement points of Xie (1981) used for the validation of the first data type = 0.05 m, 0.10 m, and 0.20 m above the flume base; for the second data type, the depths = 0.03 m (for Tests 2, 5, and 6) and 0.05 m (for the other 7 tests) above the flume base. Measurement point of Zhang et al. (2001) = ▲ (under the 1st node, $L/4$), the depth = 0.25 m above the flume base, used only for the validation of the second data type.

increase eleven times for Grid 6 and eighteen times for Grid 8 longer than the computational time of Grid 4 just for reducing the errors 1.35% and 0.82%. It makes the error reductions produced by Grids 6 and 8 are less worthy compared to the increasing of computational times.

Fig. 4 presents the comparisons of the numerical results and experimental data of Xie (1981) for the horizontal orbital velocity patterns of Test 1, Test 2, and Test 3 in Table 2. The experimental data were collected at three different depths under the 1st node and halfway of standing waves as shown in Fig. 3(b). It can be seen that the numerical results show a good agreement and consistent with the experimental data. The velocity magnitude is highest near the surface and then decreases towards the bottom. At the node, the velocity is always greater than at the halfway, which is consistent with the experimental results.

Fig. 5 presents the comparisons of the maximum velocity at the bottom, u_b, for the fourteen tests of Table 2. Fig. 5(a) and (c) compare numerical results vs. analytical solutions, while Fig. 5 (b) and (d) compare numerical results vs. experimental data (Xie, 1981; Zhang et al., 2001). The experimental data were taken under the halfway and 1st node of standing waves as described in Fig. 3. The experimental data of Xie (1981) used in these comparisons were measured at $y=0.03$ m from the wave flume base for Test 2, Test 6 and Test 5, while at $y=0.05$ m from the wave flume base for the other 7 tests, while the experimental data of Zhang et al. (2001) were measured at $y=0.25$ m above the wave flume base.

The numerical velocities at the bottom ($u_{b.n}$) under the node are close to those obtained from the theory ($u_{b.t}$) and the experiments of Xie (1981) and Zhang et al. (2001) ($u_{b.t}$) as shown in Fig. 5 (a) and (b), respectively. The percentage errors, $|\frac{u_{b.t/e}-u_{b.n}}{u_{b.t/e}}|\times 100\%$, range from 16.59% to 20.50% for Fig. 5(a) and from 11.47% to 23.64% for Fig. 5(b). On the average, $u_{b.n}=0.952u_{b.t}$ with standard deviation $\sigma=0.069$ in Fig. 5a, while $u_{b.n}=0.928\ u_{b.e}$ with $\sigma=0.065$ in Fig. 5(b). The coefficients of correlation are $\in=0.910$ for Fig. 5 (a) and $\in=0.922$ for Fig. 5(b).

The numerical velocities at the bottom under the halfway are also close to the results of theory and experiment of Xie (1981) as shown in Fig. 5(c) and (d), respectively. The percentage errors are

Table 3
The results of the grid convergence test. Wave parameters=Test 2 in Table 2. Duration=10T.

Grid	Δx (m)	Δy (m)	Total number of grid nodes	Avg. percentage errors of the 3-measurement points (%)		Avg. percentage errors of node and halfway (%)	Computational time (h)
				Node (L/4)	Halfway (L/8)		
1.	0.050	0.025	2772	11.29	12.63	11.96	1.25
2.	0.050	0.020	3276	8.04	7.50	7.77	1.50
3.	0.040	0.025	3454	9.48	9.87	9.68	1.75
4.	0.040	0.020	4082	6.33	4.70	5.52	2.25
5.	0.025	0.025	5500	4.83	9.75	7.29	14.43
6.	0.020	0.020	8424	1.83	6.50	4.17	26.55
7.	0.020	0.010	15964	4.18	7.90	6.04	37.20
8.	0.010	0.020	16524	5.76	3.64	4.70	42.30
9.	0.010	0.010	31824	9.38	13.30	11.34	47.35

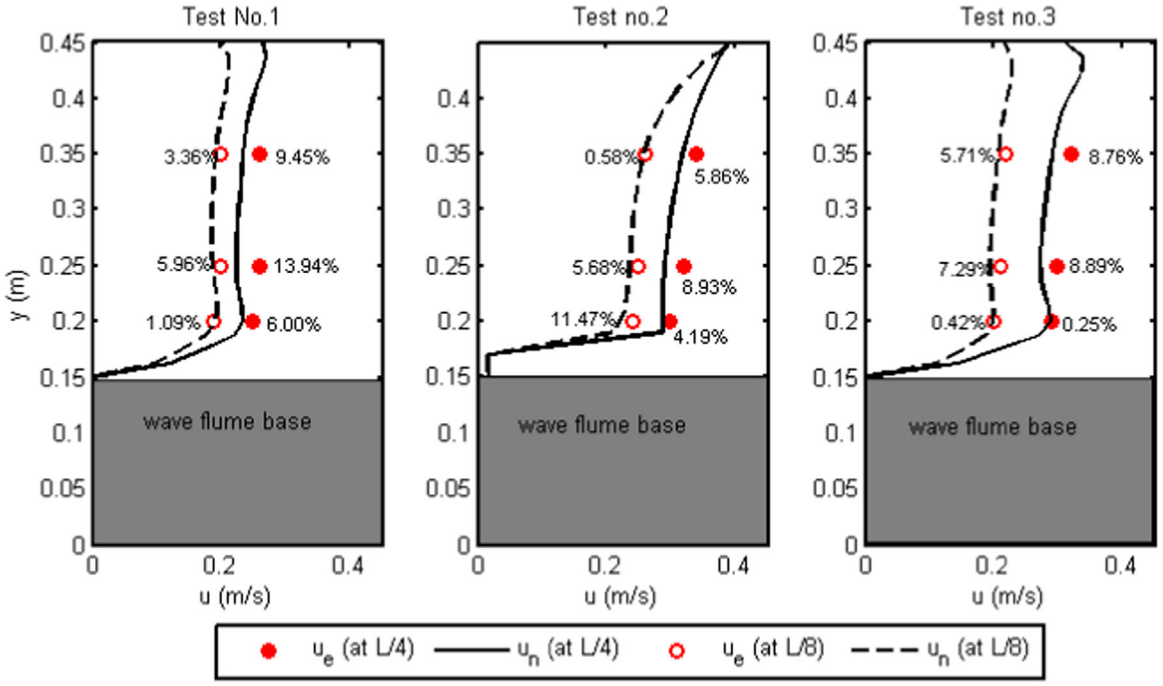

Fig. 4. Comparisons of numerical results and experimental data (Xie, 1981) for the orbital velocity patterns, u, under the 1st node (L/4) and halfway (L/8) of standing wave. Locations of measurement points are shown in Fig. 3(b) at the depths of 0.05 m, 0.10 m, and 0.20 m. Wave parameters=Test 1, Test 2, and Test 3 in Table 2. Grid size=Grid 4 in Table 3. u_e=experimental data and u_n=numerical result. Percentages are the percentage errors produced from the comparison between the numerical results and experimental data.

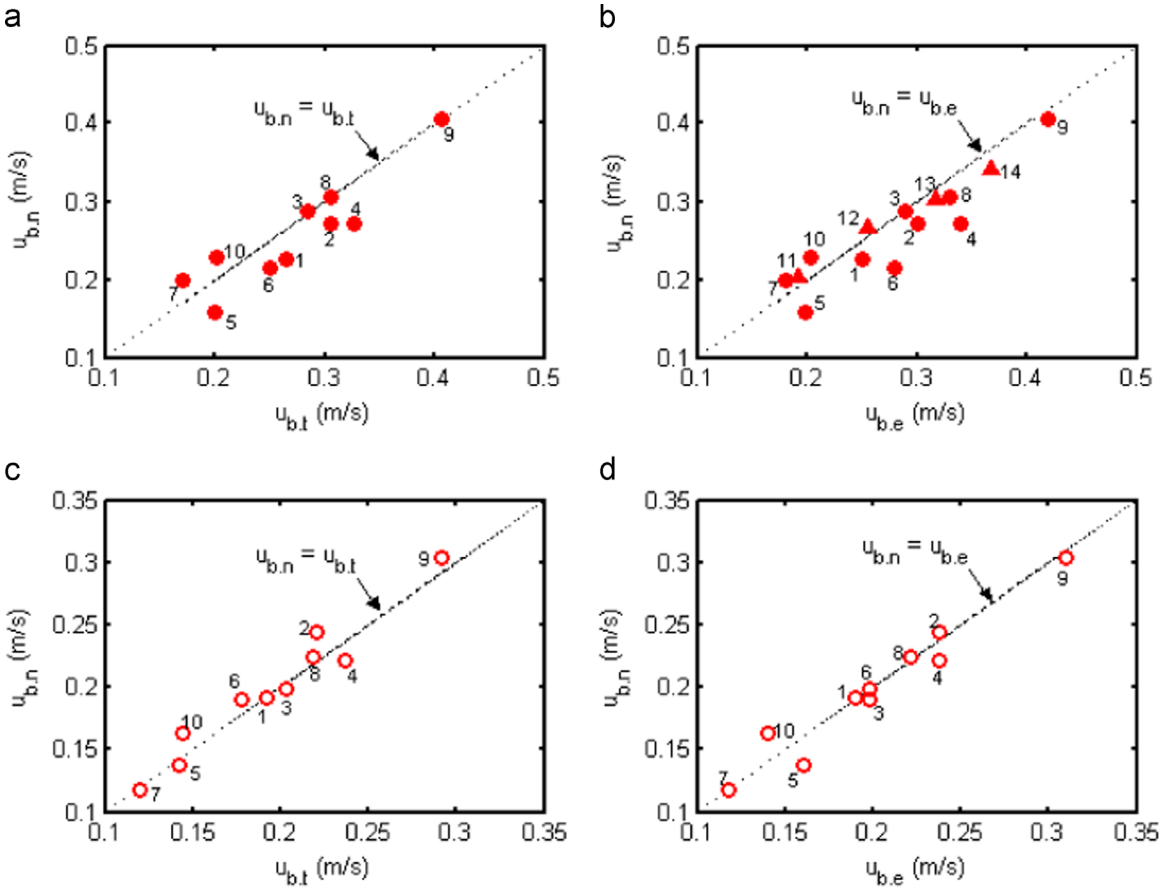

Fig. 5. Comparison of maximum velocities at the bottom, u_b: (a)–(c) numerical vs. theoretical results, (b)–(d) numerical vs. experimental data. Wave parameters are given in Table 2. Grid size=Grid 4 in Table 3. $u_{b.n}$=numerical result; $u_{b.t}$=theoretical result; $u_{b.e}$=experimental result.●=u_b measured under the 1st node, $L/4$, and ○=u_b measured under the halfway, $L/8$, based on the data of Xie (1981). ▲=u_b measured under the 1st node, $L/4$, based on the data of Zhang et al. (2001) .

ranging from 6.67% to 13.82% for Fig. 5(c) and from 13.56% to −17.07% for Fig. 5(d). On the average, $u_{b.n}=1.024u_{b.t}$ and $u_{b.n}=0.995u_{b.e}$ with $\sigma=0.0538$ for Fig. 5(c) and (d), respectively. The coefficient of correlations are $\in=0.972$ for Fig. 5(c) and $\in=0.974$ for Fig. 5(d). All these statistics describe that the numerical results have shown close agreements with both the theoretical and experimental results.

3.2. Validation of scour/deposition patterns

This study validates performance of the present model in predicting scour patterns in two tests. The simulated scour patterns offshore of vertical impermeable breakwater are validated in both tests. The first test compares the results of the present model with the experimental data of Xie (1981) and the numerical results of Tahersima et al. (2011). Table 4 presents the test conditions, following the experimental conditions of Xie (1981, experiment no. 11a, Table 1, page 8). The second test compares the present model with the experimental data of Sumer et al. (2005) and the numerical results of Gislasons et al. (2009b). Tables 5 and 6 present the test conditions, following the experimental conditions of Sumer et al. (2005) and Gislasons et al. (2009b). The comparison of the present model with the two numerical studies (Tahersima et al, 2011; Gislasons et al. 2009b) is also a way to compare the applicability of different sediment transport formulae. Tahersima et al. (2011) and Gislasons et al. (2009b) used the formulae of Engelund- Fredsøe (1976) and Bijker (1971), which are based on the deterministic approach that uses the instantaneous velocities as the input. Meanwhile, the present model uses the formula of Bailard (1981), which is based on the energetic approach that uses the time-averaged velocities as the input.

Table 4
Test conditions based on the experiment of Xie (1981).

Breakwater	d(m)	H_i (m)	L (m)	T (s)	D_{50}(μm)	ρ_s(kg/m^3)	w(m/s)
Vertical (impermeable)	0.3	0.05	1.714	1.17	150	2650	0.05

Table 5
Test conditions based on the experimental conditions of Sumer et al. (2005) and Gislason et al.(2009b).

Breakwater	d (m)	H_i (m)	L (m)	T (s)	d/L
Vertical (impermeable)	0.31	0.02	3.3	2	0.094

Table 6
Sediment properties (Sumer et al., 2005; Gislason et al, 2009b).

Parameter	Φ	ε_b	ε_s	ρ_s (kg/m^3)	w (m/s)	D_{50} (mm)	p
Value	31°	0.1	0.02	1130	0.02	0.44	0.4

For the first test, Xie (1981) observed that the scouring pattern developed under the conditions presented in Table 4 was resembling the reference pattern of coarse material (Fig. 6). In the reference pattern, the scour troughs occur under the halfway ($L/8$, $3L/8$, and $5L/8$ from the breakwater) and the deposition ridges

occur under the node of the standing waves ($L/4$ and $3L/4$ from the breakwater). Please refer to (Xie, 1981, Table 11, page 20) for the details. Therefore, the simulated scouring pattern must also show the same pattern as observed in the experiment.

The maximum equilibrium scour depth and the time scale required to reach it are two quantities of large practical importance. According to the experimental data of Xie (1981) for coarse material, the time required to reach the maximum equilibrium scour depth was about $7000T$ for $H/L > 0.02$, and about $6500T$ to $10{,}000T$ for $H/L < 0.02$, dependent on the relative water depth d/L. For the same value of H/L, it was found that the required time increased as the value of d/L increased. Xie (1981) also gave the following empirical expression for the maximum equilibrium scour depth in the case of vertical breakwater with coarse material:

$$\frac{S}{H} = \frac{0.3}{\left(\sinh\left(\frac{2\pi d}{L}\right)\right)^{1.35}} \tag{25}$$

where S is the maximum equilibrium scour depth.

Based on the test conditions given in Table 4, the relative wave height, $H/L = 0.029$, and the relative water depth, $d/L = 0.175$. Using Eq. (25), it is found that the maximum scour depth for this test condition is $S = 1.0$ cm with $S/H = 0.20$. Unfortunately, Xie (1981) did not clearly describe the data of time scale required to reach this maximum scour depth. However, based on the experimental results of Xie (1981) as described above, it is believed that more than $7000T$ are required to reach the maximum equilibrium scour depth.

The scour patterns simulated by Tahersima et al. (2011) and the present model are described in Fig. 7, in which the x-axis is normalized by the wavelength (L). As shown in Fig. 7(a), the scour/deposition pattern of Tahersima et al. (2011) is not following the reference pattern shown in Fig. 6. Meanwhile, the scour/deposition pattern of the present model (Fig. 7(b)) accurately resembles the pattern of Fig. 6. It is also found that the maximum scour depth simulated by the present model is $S = 1.1$ cm with $S/H = 0.21$, which is reached after $O(10000)T$. The predicted maximum scour depth is equal to the experimental data of Xie (1981). In addition, the time scale required to reach the maximum scour depth is also consistent with the trend found in the experiment of Xie (1981). These results show that the present model is able to predict the scour/deposition pattern better than the numerical result of Tahersima et al. (2011).

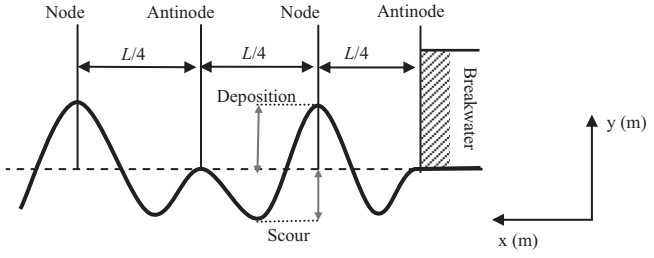

Fig. 6. Description of scour/ deposition pattern for coarse material of Xie (1981).

In the second test, the present model was compared to the experimental data of Sumer et al. (2005) and the numerical results of Gislason et al. (2009b). The test conditions and sediment properties used in this comparison were set similar to the studies of Gislason et al. (2009b) and Sumer et al. (2005). The test conditions are presented in Table 5 with breakwater type is vertical impermeable and the sediment used for this test is Acrylic with the properties as given in Table 6.

Fig. 8 shows the comparison between the experimental data of Sumer et al. (2005), the results of present model, and the numerical results of Gislason et al. (2009b). It can be seen that both models can produce scour/deposition patterns consistent with the experimental data as shown in Fig. 8(b) and (c). For this test condition, Sumer et al. (2005) stated that the maximum equilibrium scour depth relative to the incident wave height, $S/H = 0.50$ or $S = 1.1$ cm with $S/H = 0.57$ (as if calculated by Eq. (25)), which was reached after $O(1200)T$. Meanwhile, Gislason et al. (2009b) found that $S/H = O(1)$ that was reached with longer duration $O(10000)T$. This simulated maximum scour depth is two times greater than the experimental data. The present model simulates that the maximum scour depth is $S = 1.1$ cm with $S/H = 0.57$, which is equal to the experimental data of Sumer et al. (2005). However, this predicted maximum scour depth is reached after $O(17000)T$, longer than the experimental data and the numerical result of Gislason et al. (2009b). There is no clear explanation for these time scale discrepancies. Gislason et al. (2009b) stated that these discrepancies may be partly explained by the ripples which are presented in the experiments, but not in the both models.

Fig. 9 presents the time development of scour depths at the location nearest to the toe of breakwater for both tests (Fig. 7, for the first test, and Fig. 8, for the second test). In this figure, the relative scour depth, S/H, is plotted versus time that is expressed as $t = NT$, in which N is the number of waves and T is the wave period. It is seen in both tests that the relative scour depths increase rapidly in the beginning. Their values reach half of the ultimate values of S/H in between of $O(2000)T$–$O(3000)T$, and then continue to develop with decreasing rate until reaching the equilibrium depth at $O(10{,}000)T$ for the first test (Fig. 7) and $o(17{,}000)T$ for the second test (Fig. 8). Fig. 9 also shows that the present model is able to capture that the scour develops from the

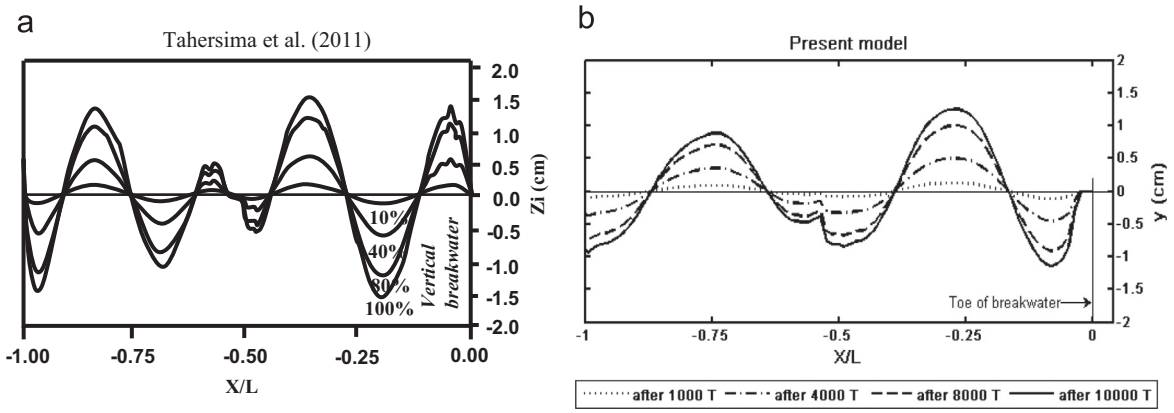

Fig. 7. Scour/deposition patterns in equilibrium state: (a) the numerical result of Tahersima et al. (2011) and (b) the result of present model.

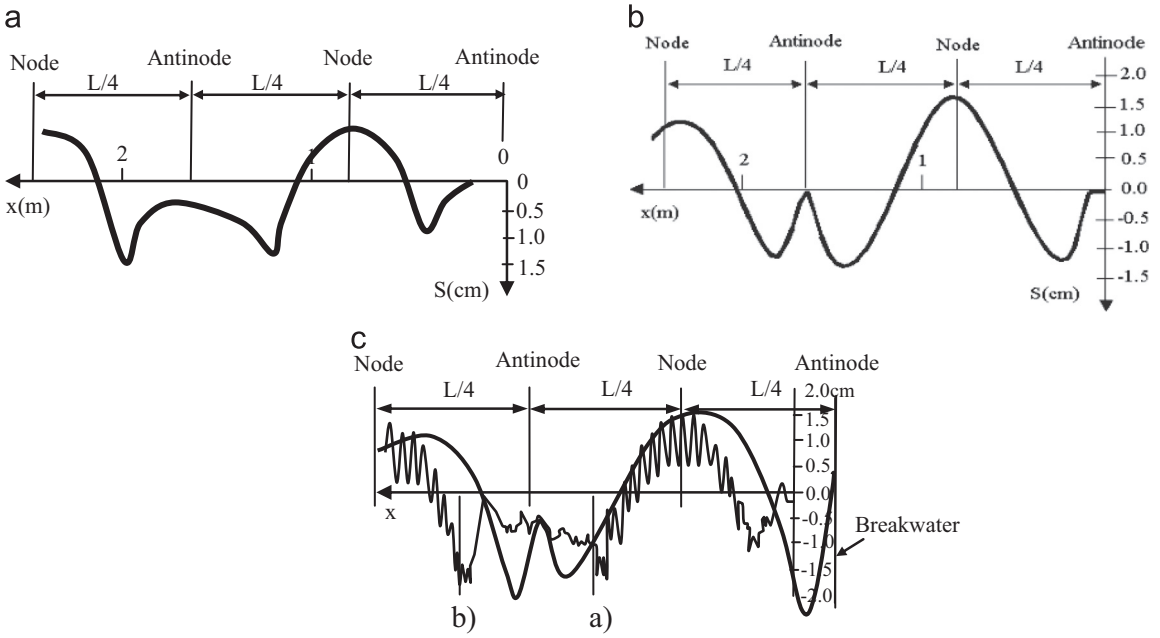

Fig. 8. Scour/deposition patterns offshore of vertical impermeable breakwaters. (a) The result of Sumer et al. (2005) obtained after $O(1200)T$, (b) The result of present model obtained after$O(17000)$ T and (c) the result of Gislason et al. (2009) obtained after $O(10{,}000)T$ (**thick line**: numerical simulation; **line with ripples**: the experimental data).

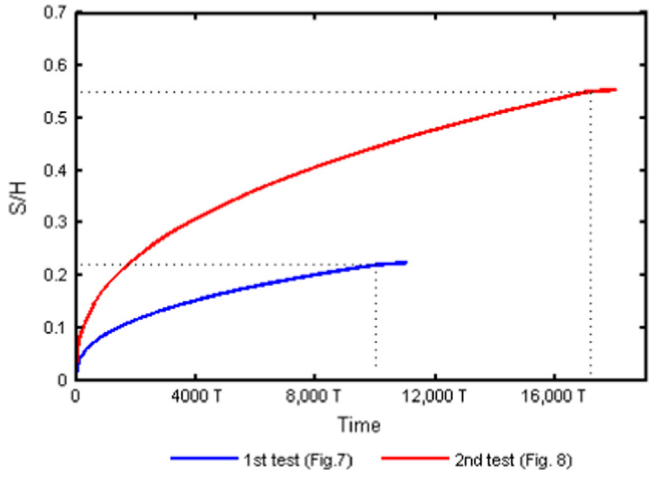

Fig. 9. Time development of scour depth at location nearest the breakwater of the two tests.

bed profile, which is initially flat, until reaching equilibrium profile.

4. Results of numerical experiments

4.1. Non-overtopping vs. overtopping

Wave overtopping is of principal concern for breakwaters constructed primarily for coastal protection. Zhang et al. (2001) and Yeganeh-Bakhtiary et al. (2010) have shown that wave overtopping affects the dynamic characteristics of standing waves offshore of vertical breakwaters. It is then predicted to affect the development of scour at the seabed as well. Undesired scour/deposition of the seabed offshore of the breakwater can be a serious threat for the breakwater stability. Although Tahersima et al. (2011) tried to simulate scouring under the effect of overtopping, but their simulation results are not consistent with the reference pattern of Xie (1981). So that, there is still a gap of knowledge in regard to the connections between the wave overtopping and scour development offshore of vertical breakwaters.

Table 7
Simulation conditions, the simulated mean wave height and period, and overtopping discharge.

Test	H_i (m)	L (m)	T (s)	d (m)	R_c (m)	H_m (m)	T_p (s)	q (m^3/s/m)
Run 1	0.085	2.400	1.530	0.30	No	0.138	1.524	–
Run 2	0.075	2.400	1.530	0.30	0.00	0.088	1.521	0.0051
Run 3	0.085	2.400	1.530	0.30	0.00	0.098	1.519	0.0059
Run 4	0.095	2.400	1.530	0.30	0.00	0.108	1.529	0.0069
Run 5	0.110	2.400	1.530	0.30	0.00	0.122	1.526	0.0082
Run 6	0.075	2.400	1.530	0.30	0.02	0.105	1.515	0.0026
Run 7	0.085	2.400	1.530	0.30	0.02	0.118	1.512	0.0032
Run 8	0.095	2.400	1.530	0.30	0.02	0.129	1.527	0.0039
Run 9	0.110	2.400	1.530	0.30	0.02	0.145	1.524	0.0048
Run 10	0.085	2.400	1.530	0.30	0.06	0.120	1.535	0.0014

*R_c = freeboard; H_m = the mean wave height at the toe; T_p = the mean wave period at the toe ; q = the overtopping discharge.

To bridge this gap, two simulations (Run 1 and Run 3 in Table 7) were conducted to investigate the effects of overtopping on the hydrodynamics and scouring offshore of a vertical breakwater. The simulations were conducted in a 7 m × 1 m numerical wave flume with d (water depth) = 0.3 m, using the same wave condition. A vertical impermeable breakwater was placed at the right boundary with no freeboard in the non-overtopping case (Run 1) and zero freeboard (R_c = 0.0 m) in the case of overtopping (Run 3). Waves were generated by the Dirichlet-type wave maker at the left boundary, 6.12 m away from the breakwater. The computational domain is shown in Fig. 1 and the sediment properties were set similar to those in Table 6. The duration of simulations was set for 17,000 T, which was following the time required to reach equilibrium states as in Section 3.2.

Fig. 10 presents the snapshots of wave profiles offshore of the breakwater during its interaction with the breakwaters. All figures were captured within the time range of 5.4T–7.7T. This was the time when the 4th incident wave was approaching to (Fig. 10 (a) and (d)), impinging on (Fig. 10(b) and (e)), and reflected from the breakwater (Fig. 10(c) and (f)). In this time range, the standing waves were already formed offshore of the breakwater, which

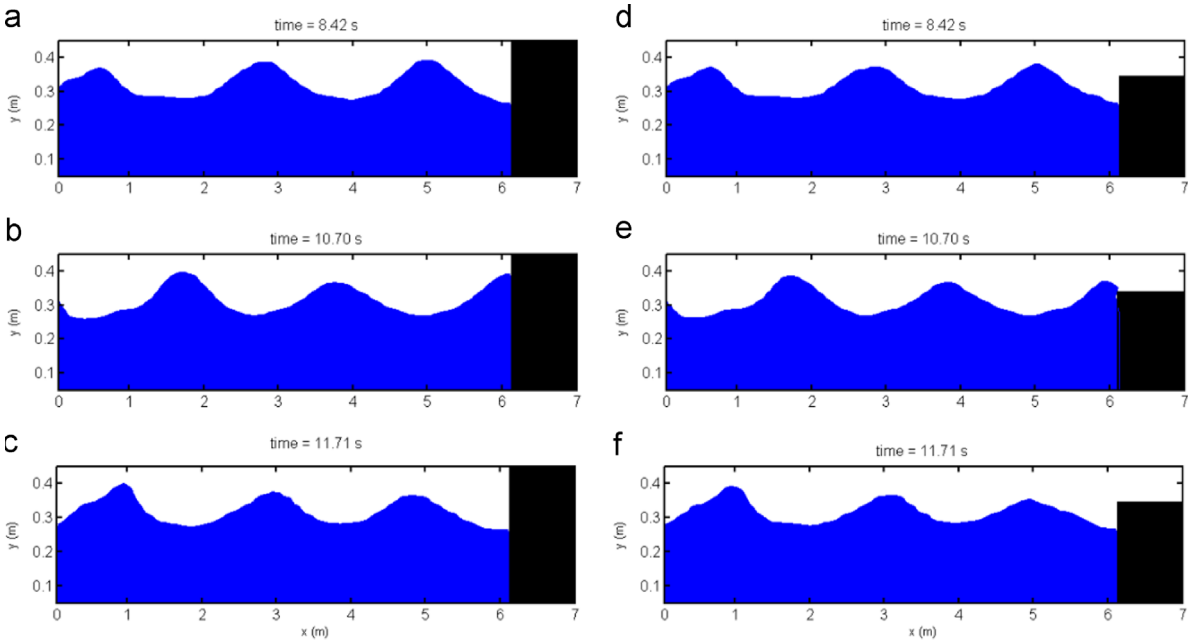

Fig. 10. Snapshots of wave profile offshore of the breakwater. (a)–(c) Non-overtopping case and (d)–(f) overtopping case.

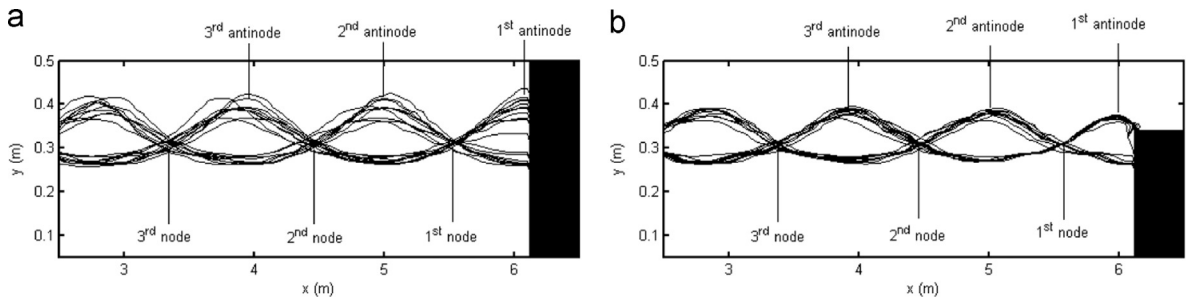

Fig. 11. Standing wave profiles offshore of the breakwater during 3*T*–20*T*. (a) Non-overtopping case and (b) overtopping case.

were fully standing waves in the case of non-overtopping (Fig. 10 (a)–(c)) and partially standing waves in the case of overtopping (Fig. 10(d)–(f)).

The comparison of two cases in Fig. 10 shows that overtopping occurrence changes the characteristics of reflected waves and thus the characteristics of standing waves. In the case of non-overtopping, almost all energy of the incident wave is reflected back after the wave impinged on the breakwater. The reflected waves then superpose with the next incident wave. At this time, the both waves carry energies that are nearly balanced. Their superposition finally generates a resultant wave offshore of the breakwater that seems more symmetric in profile and higher in amplitude as shown in Fig. 10(c). In the overtopping case, the energy of the incident wave is partly transmitted to the crown of the breakwater and partly reflected back by the breakwater. In front of the breakwater, the reflected and the next incident waves, which carry energy with different level, then superpose and result in a resultant wave that seems slightly asymmetrical in profile and lower in amplitude as shown in Fig. 10(f). This process occurs repetitively and eventually develops standing waves offshore of the breakwater.

Fig. 11 depicts the profiles of standing waves in both cases. These profiles were attained as the wave surface reached its extreme positions that occurred twice in every wave period. For clarity, they were taken only at 3*T*, 3.5*T*, 4*T*, 4.5*T*, … , 19*T*, 19.5*T*, and 20*T*. In both cases, the nodes and antinodes of standing waves are formed at similar positions. The first nodes are located around 0.6 m and the second antinodes are at around 1.12 m away from the breakwater. However, wave amplitude in Fig. 11(a) is higher than in Fig. 11(b). This result indicates that the energy and the symmetrical behavior of standing waves decrease due to overtopping.

Changes in the characteristics of standing waves due to overtopping consequently generate different scour/deposition patterns at the bottom. Fig. 12 shows bed profiles and the distributions of total sediment transport rate (S_T) and its gradient. The bed profiles clearly follow the reference patterns of Xie (1981) and Sumer et al. (2005) as in Figs. 6 and 8(a), respectively. These profiles were obtained after applying the incident waves for 17,000*T*. The sizes of scour depths/deposition heights in the case of overtopping are generally smaller than in the case of non-overtopping. Interestingly, there is only very small scour at the toe of the breakwater as overtopping occurs, which means less threat to the breakwater stability.

Tofany et al. (2014) have shown that direction of sediment movement can be tracked by relating the spatial distribution of S_T with locations of the developed scour troughs/deposition ridges. Using this approach, the sediment movement is tracked as shown by the black arrows in Fig. 12(b) and (d). Low sediment movement is seen in the area close to the toe of breakwater when overtopping occurs, Fig. 12(d). This explains why there is only small scour developed at the toe of the breakwater in Fig. 12(c).

Changes of steady streaming due to overtopping are the inducing mechanism for different scour/deposition patterns observed in Fig. 12(a) and (c). The steady streaming is a system of re-circulating cells generated under the surface of standing wave. Fig. 13 plots the

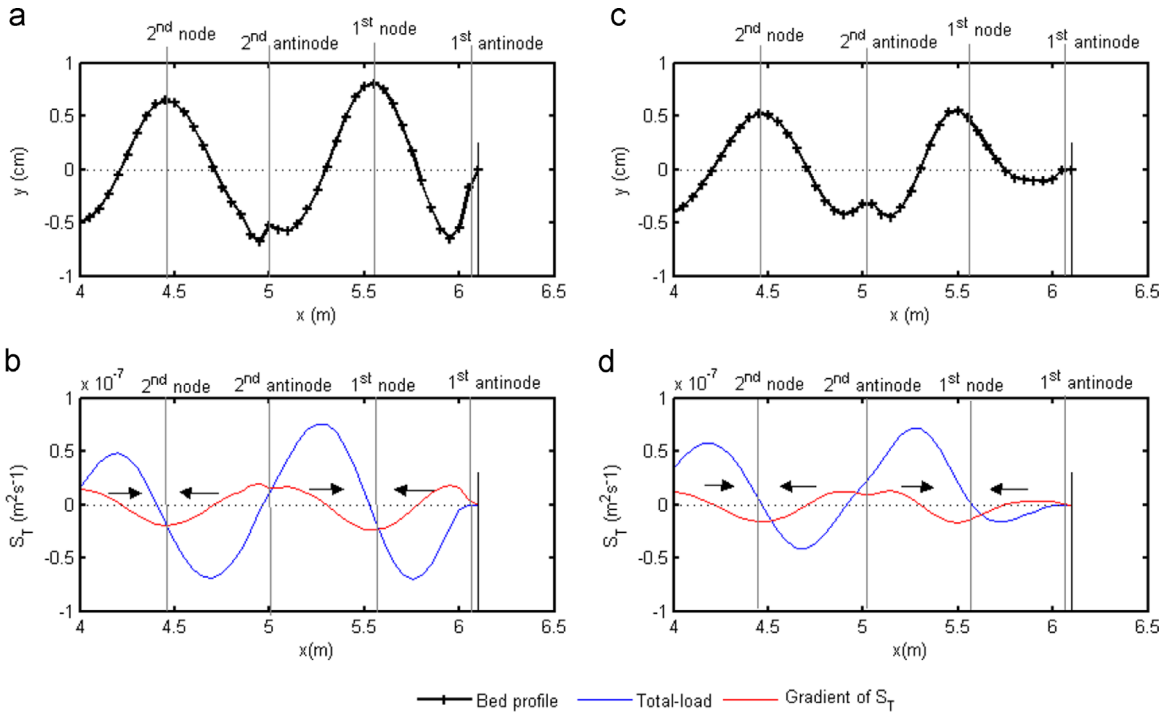

Fig. 12. Bed profiles and spatial distribution of total transport rate (S_T) and its gradient offshore of the breakwater. (a) and (b) non-overtopping case, (c) and (d) overtopping case.

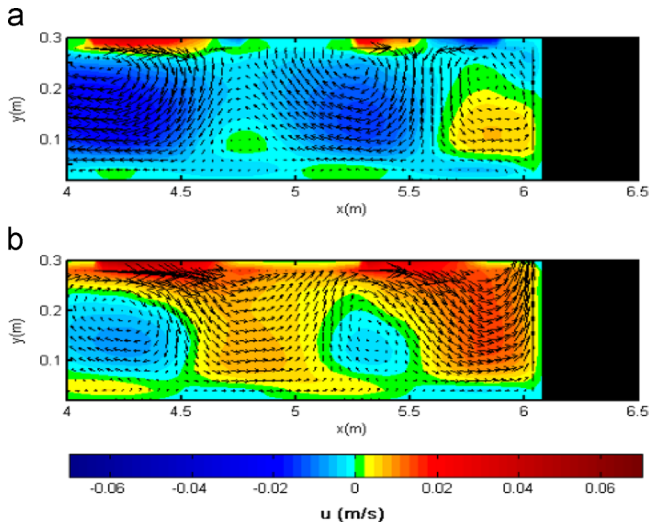

Fig. 13. Steady streaming and distribution of horizontal velocity. (a) Non-overtopping case and (b) overtopping case. The colormap represents the magnitude of the averaged horizontal velocity u (m/s).

re-circulating cells of steady streaming and distribution of horizontal velocity magnitude (in meter per second) in both cases. All parameters in the plots have been averaged over the duration of simulation (17,000T). Profiles of re-circulating cells in Fig. 13 (a) are relatively more apparent than in Fig. 13(b). Two re-circulating cells in the opposite direction are formed around the first node of the standing waves. These cells induce sediments to move from the 1st and 2nd antinodes of standing wave toward the 1st node and finally deposited there (Fig. 12(a) and (b)). The substantial scour at the toe of breakwater (Fig. 12(a)) is induced by the anticlockwise cell that formed right in front of the breakwater. The profile of re-circulating cells changes when overtopping occurs (Fig. 13(b)). Right in front of the breakwater, fluid particles mostly flow in the right direction, towards the breakwater crown and no re-circulating cell is generated near the toe. Right in front of the toe and at the bottom, there is observed small intensity flow to the left direction. Two possible mechanisms may contribute in generating this flow. Firstly, from the separation of fluids at the bottom with the upper fluids, in which the bottom fluids do not flow up to the crown of breakwater but reflected by the breakwater. Secondly, from the return flow of fluids flowing down the breakwater from the crown after overtopping. However, based on Fig. 12(d), the intensity of this flow is weak that move only a small amount of sediment from the 1st antinode towards the 1st node. This explains why there is no substantial scour at the toe when overtopping occurs.

Fig. 14 presents the spatial distribution of the time-averaged turbulence parameters in the case of overtopping. In the present model, the magnitude of eddy viscosity is representing the scale of turbulence in the flow field. Fig. 14(a) and (b) shows that most of the turbulence kinetic energy and its dissipation rate are generated locally on the crown of the breakwater. However, their scales of magnitudes are sufficiently small to affect the mean flow. It is indicated by the magnitude of eddy viscosity in Fig. 14(c), which is very small to change the flow into turbulent. In addition, this small turbulence is restricted only on the crown and does not spread into area offshore of the breakwater. It indicates that the structure of steady streaming and thus the sediment transport offshore of the breakwater are not affected by the turbulence generated on the crown. Similar patterns of turbulence parameters are also observed in all tests conducted in this article that involves overtopping (Run 2–Run 10 in Table 7), they slightly differ only in terms of magnitude.

4.2. Overtopping with different discharges

The results presented in the previous section have shown that overtopping occurrence clearly affects the hydrodynamics and scour pattern offshore of the breakwater. This section presents and discusses the results of numerical experiments that are conducted to investigate the hydrodynamics and scour pattern when overtopping

occurs with different discharges. Two factors were considered as the mechanisms that change the overtopping discharge. They were wave condition and breakwater height (freeboard). Table 7 enumerates the detailed simulation conditions. Computational domain and boundary conditions are the same as depicted in Fig. 1, while sediment properties are presented in Table 6.

Fig. 15 presents snapshots of wave profiles in time of 30.62 s, which is one of the moments when overtopping occurs in the simulation, and compares the mean overtopping discharges (q) of Run 2–Run 9. These Runs were performed using four different incident wave heights, namely $H_i = 0.075$ m, 0.085 m, 0.095 m, and 0.110 m, and separated into two groups based on the freeboard

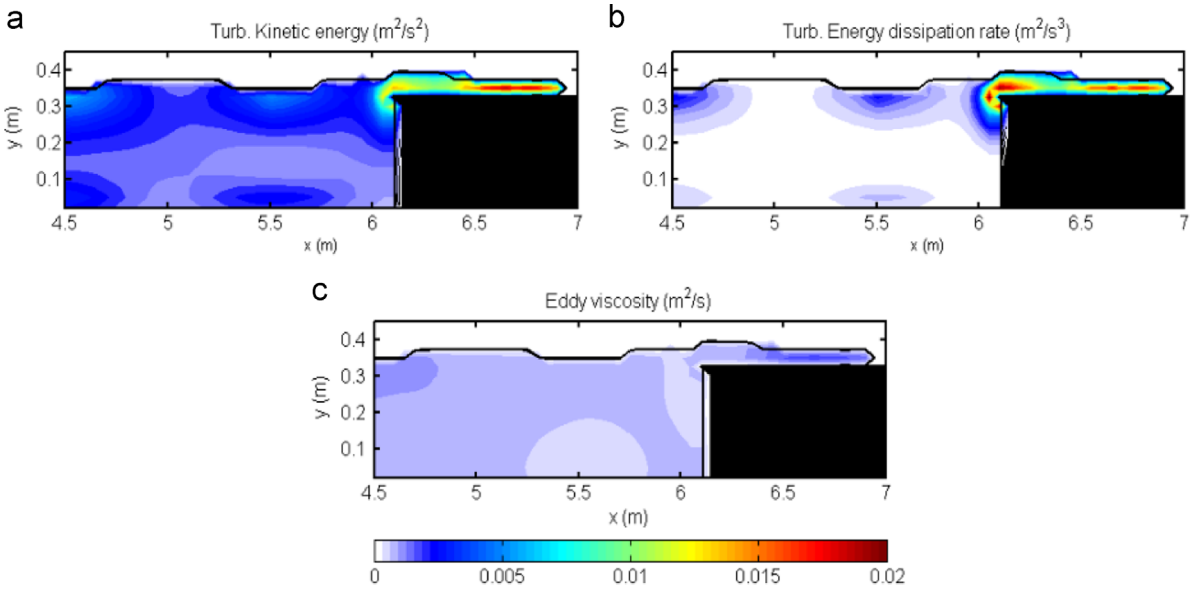

Fig. 14. Spatial distribution of time-averaged turbulence parameters offshore of the breakwater in the overtopping case.

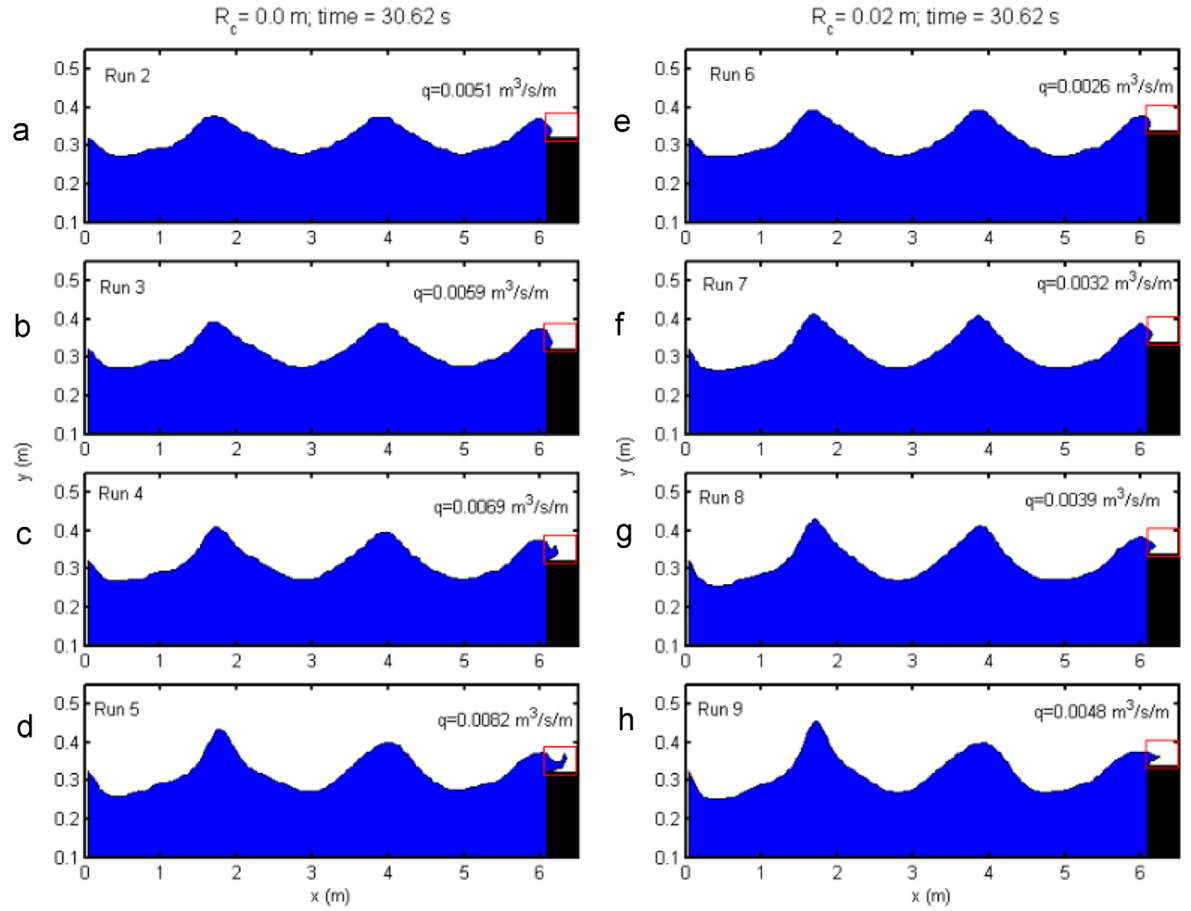

Fig. 15. Snapshots of wave profiles offshore of the breakwater at the moment when overtopping occurs. (a)–(d) Run 2–Run 5, (e)–(h) Run 6–Run 9. q is the mean overtopping discharge.

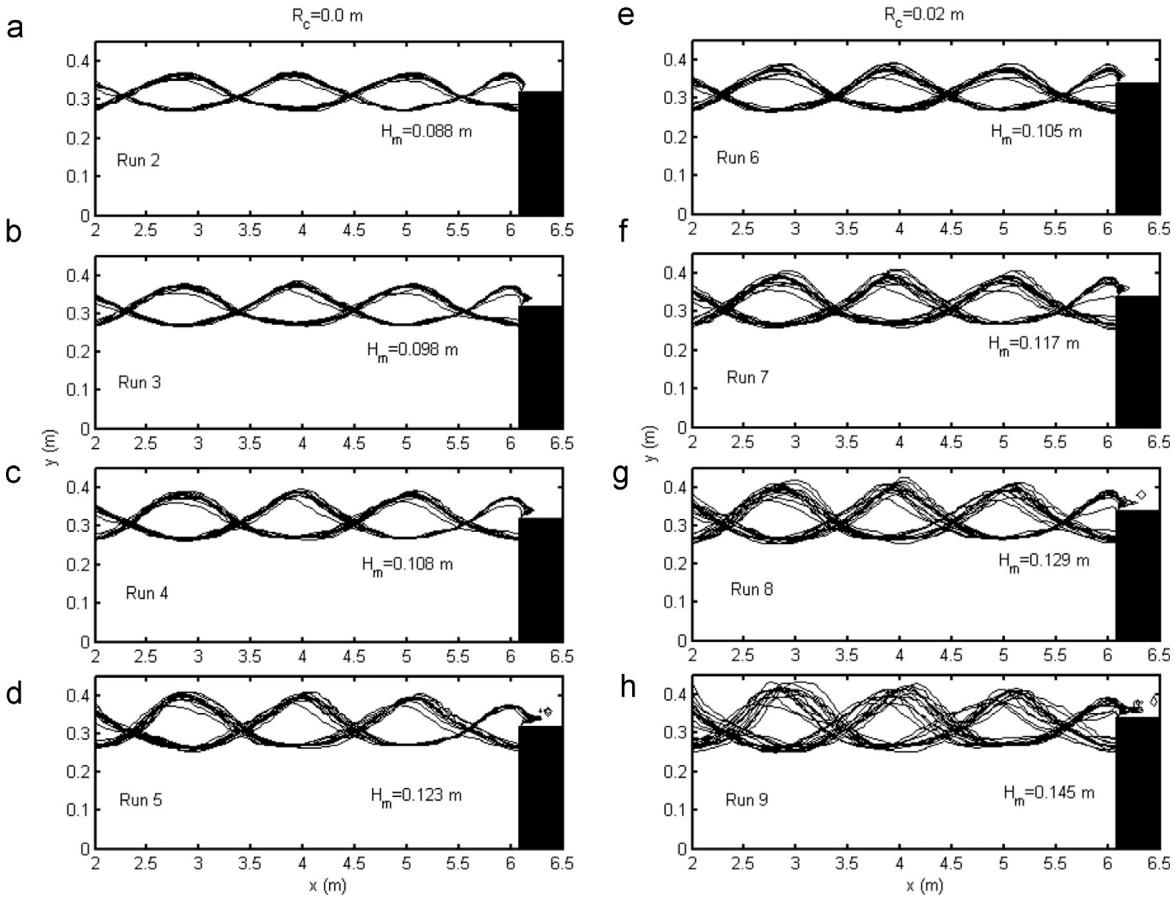

Fig. 16. Standing wave profiles offshore of the breakwater. (a) Run 2, (b) Run 3, (c) Run 4, (d) Run 5, (e) Run 6, (f) Run7, (g) Run 8, and (h) Run 9. H_m is the mean wave height.

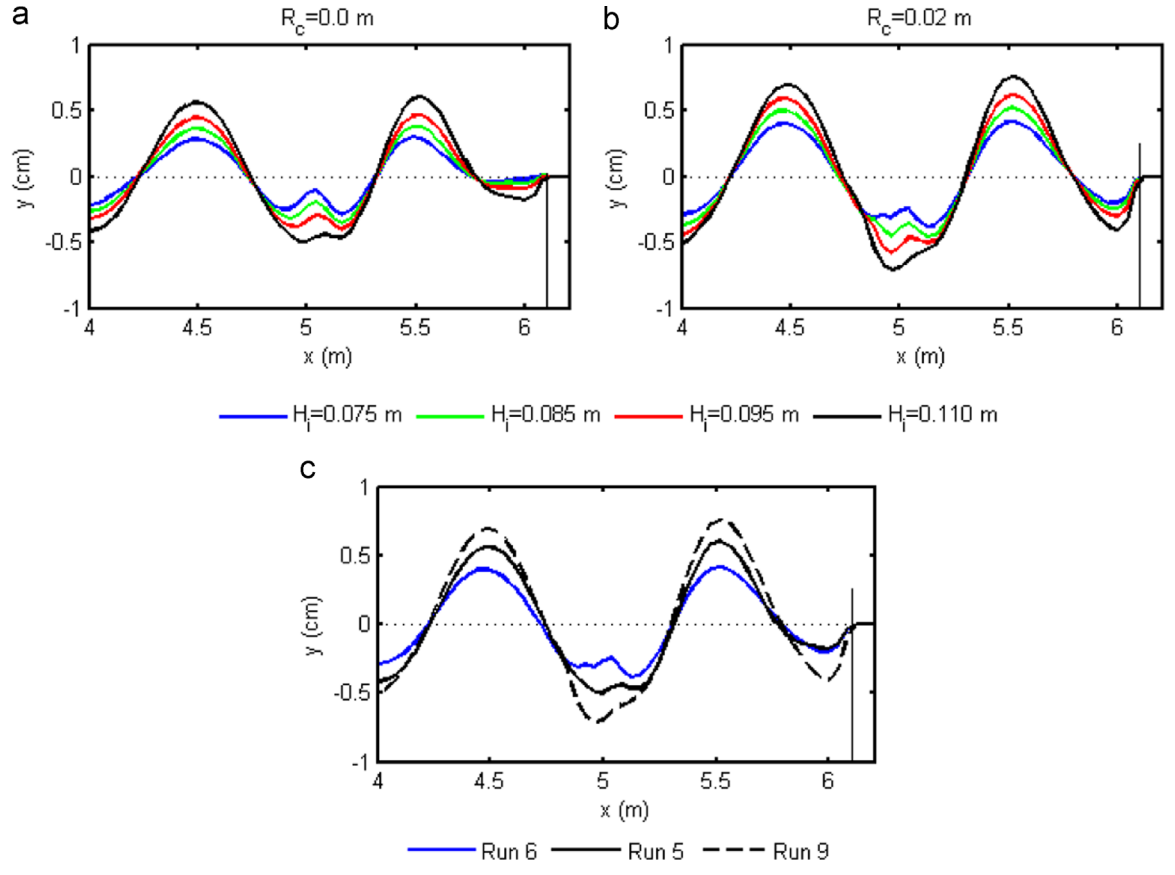

Fig. 17. Bed profiles offshore of the breakwater for different incident wave heights (H_i) and freeboards. (a) R_c = 0.0 m, (b) R_c = 0.02 m, (c) Run 5 vs. Run 6 vs. Run 9.

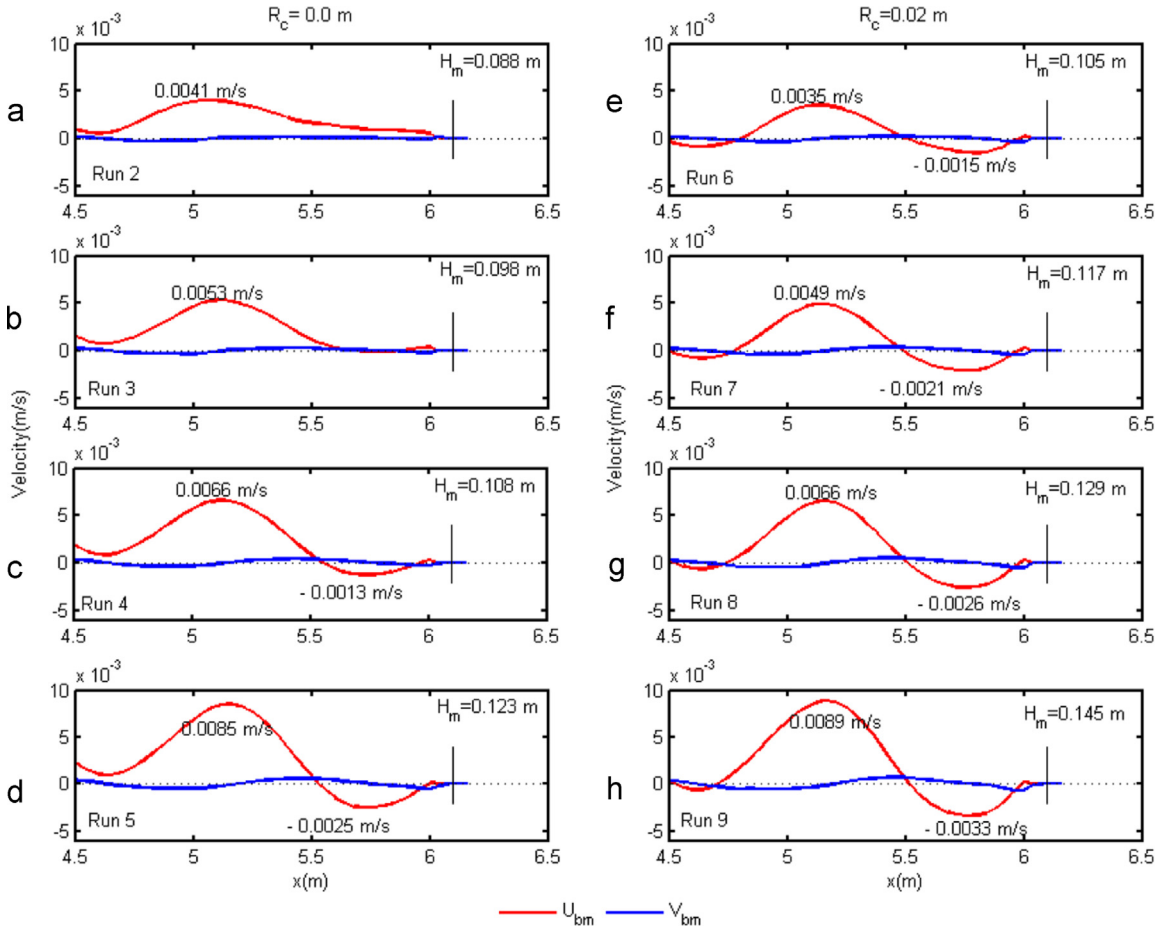

Fig. 18. Spatial distribution of the mean velocities at the bottom ($y=0.02$ m) for different wave conditions and freeboards. U_{bm} is the horizontal velocity, V_{bm} is the vertical velocity, H_m is the mean wave height, and q is the overtopping discharge.

(R_c). The first group consists of Run 2–Run 5, which is the zero freeboard group ($R_c=0.0$ m), and the simulated wave profiles are presented in Fig. 15(a)–(d). The second group consists of Run 6 – Run 9 with $R_c=0.02$ m and the simulated wave profiles are presented in Fig. 15(e)–(f). The values of q were calculated manually using the empirical equations of non-impulsive waves for plain vertical breakwaters. These equations were taken from European Overtopping Manual (Pullen et al., 2007), equation 7.3, page 136 for the cases of breakwater with freeboard (the second group) and equation 7.5, page 137 for the cases of breakwater with zero freeboard (the first group). The non-impulsive formula was used because there was no breaking (impulsive) wave observed in all simulations conducted in this study.

In each group (the same freeboard), the overtopping discharge increases with the increasing of incident wave height. It can be seen qualitatively in the red boxes and quantitatively through the q values in Fig. 15. Furthermore, when both groups are compared to each other, it is seen that the q values of the second group are around half of the q values of the first group. These results show that wave height and freeboard affect the overtopping discharge. In turn, they will affect the hydrodynamics and scour pattern offshore of the breakwater as will be shown later.

The increasing overtopping discharge implies that the portion of wave energy that is transmitted to the crown of breakwater increases, causing the reflected wave is generated with lower energy level. Furthermore, the amplitude of the reflected wave becomes smaller as the discharge increases, which subsequently affects profile of the resultant standing wave. Fig. 16 presents the profiles of the resultant standing waves in Run 2–Run 9. These profiles were plotted only at $3T$, $3.5T$, $4T$, $4.5T$, …, $19T$, $19.5T$, and $20T$. A general trend that can be drawn from Fig. 16 is that the height of the resultant standing wave increases as the height of the incident wave increases and the higher freeboard is installed in the domain. It is shown quantitatively by the calculated mean wave height (H_m). The profiles of standing waves also look becoming more asymmetrical as these two parameters increase.

The change of standing wave profile subsequently has implications to flow condition under the surface and the resultant scour pattern at the bottom. Fig. 17(a) and (b) compare the bed profiles of the first group (Run 2–Run 5) and the second group (Run 6–Run 9). In each group (the same freeboard), a same trend can be observed that the higher wave generates higher deposition ridge and deeper scour. The effect of different freeboard also looks significant in changing the scour/deposition pattern, especially to the scour depth nearest to the toe of the breakwater. This scour, usually called as the toe scour, is the main part of the entire scour/deposition pattern under consideration because it can affect the breakwater stability. As shown before, the overtopping discharges of the cases of zero freeboard are higher compared to the cases with freeboard. Meanwhile, it can be seen in Fig. 17(a) that the depths of the toe scour in the cases of zero freeboard are shallower compared to those in the cases with freeboard. This indicates that there is also a connection between the increasing of overtopping discharge and the decreasing of the developed scour pattern at the bottom.

Fig. 17(c) compares the resultant bed profiles of Runs 5, 6, and 9. Run 5 and Run 9 have the same incident wave height ($H_i=0.110$ m), which is higher than the one in Run 6 ($H_i=0.075$ m). However, the freeboard of Run 5 ($R_c=0.00$ m) is lower than the freeboard of Runs

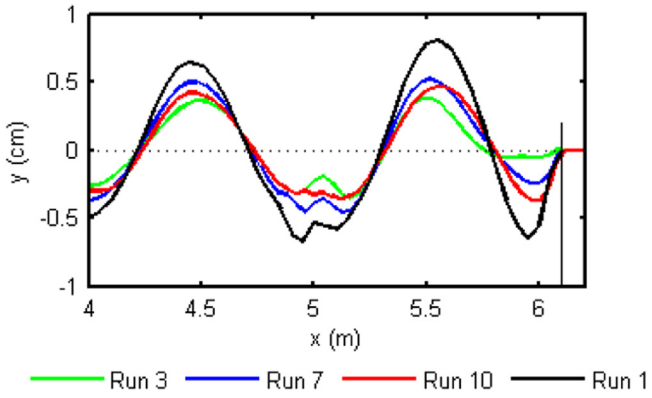

Fig. 19. Bed profiles for different freeboards with the same wave condition.

Table 8
The results of the simulation of different freeboards.

Test	H_i (m)	L (m)	T (s)	d (m)	R_c (m)	H_m (m)	T_p (s)	q (m^3/s/m)
Run 3	0.085	2.400	1.530	0.30	0.00	0.098	1.519	0.0059
Run 7	0.085	2.400	1.530	0.30	0.02	0.118	1.512	0.0032
Run 10	0.085	2.400	1.530	0.30	0.06	0.120	1.535	0.0014
Run 1	0.085	2.400	1.530	0.30	No	0.138	1.524	–

*R_c=freeboard; H_m=the mean wave height at the toe; T_p=the mean wave period at the toe ; q=the overtopping discharge.

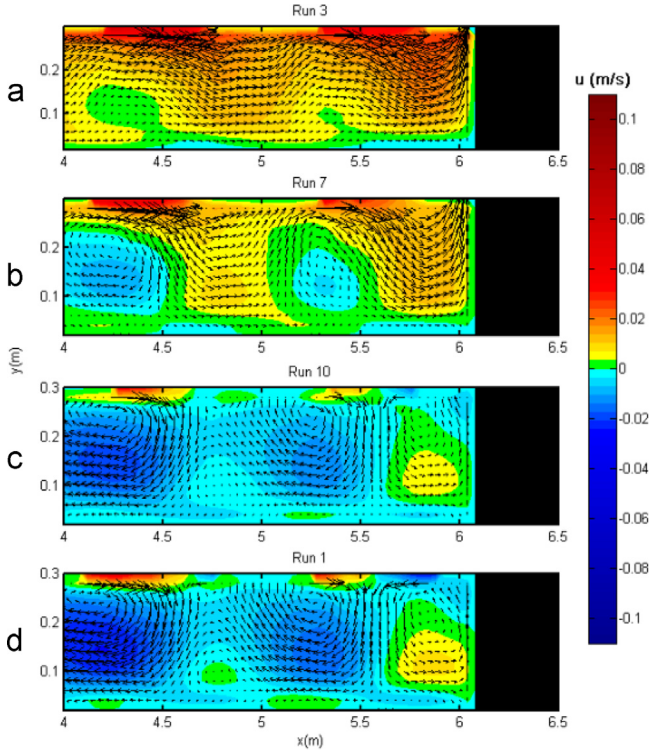

Fig. 20. Steady streaming and distribution of horizontal velocity for different freeboards. The colormap represents the magnitude of the averaged horizontal velocity, u (m/s).

6 and 9 (R_c=0.02 m), causing overtopping discharge greater than the others as shown in Fig. 15. It is interesting to see how the depth of toe scour in Run 5 is equal to the one in Run 6. If it is assumed that there was no change in the freeboard, the bed profile when H_i=0.110 m and R_c=0.02 m is supposed to be the one shown by the dashed line in Fig. 17(c). Once again, this result clearly shows

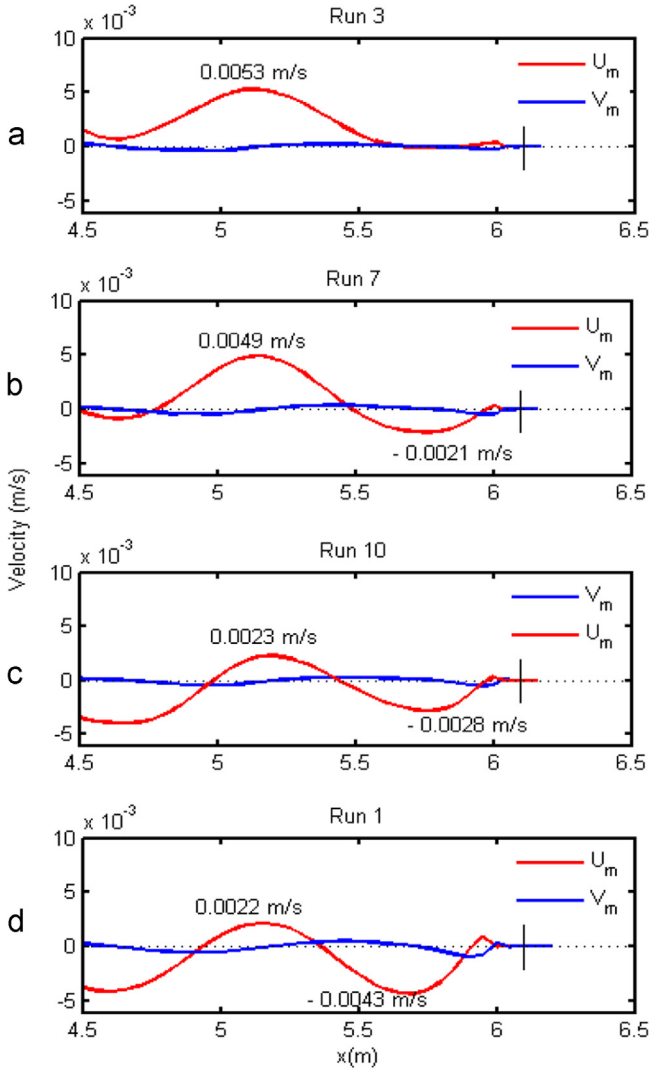

Fig. 21. Spatial distribution of the mean velocities at the bottom (y=0.02 m) for different freeboards. U_{bm} is horizontal velocity, V_{bm} is vertical velocity.

that the effect of freeboard is significance in changing the developed scour at the bottom, in which lower freeboard increases the overtopping discharge and eventually reduces the depth of toe scour.

Fig. 18 shows the spatial distribution of the averaged horizontal and vertical velocities at the bottom (y=0.02 m), U_{bm} and V_{bm}, respectively. In the figure, positive value shows that flow direction is to the right towards the breakwater, while negative value is the vice versa. At the bottom, fluids mostly flow horizontally from antinodes and converge at nodes. In each group (the same freeboard), it is seen either qualitatively or quantitatively that the magnitude of U_{bm} increases with the increasing of H_m, while the magnitude of V_{bm} remains close to zero. The comparison between the two groups shows that higher freeboard amplifies the magnitude of U_{bm}. In relation to the resultant toe scours presented in Fig. 17(a) and (b), the results presented in Fig. 18 show that the root cause of the deepening of the toe scour in Fig. 17(b) is clearly due to the amplification of U_{bm} at the halfway between the 1st antinode and 1st node of the standing wave or around x=5.75 m in the figure.

Additional analysis of the effects of different freeboard on the toe scour and the flow condition offshore of the breakwater was carried out and the results are presented here. Four Runs consisting of three breakwaters with different freeboards (Runs 3, 7,

and 10) and one breakwater without freeboard (Run 1) were compared, in which the wave condition for all these Runs is set to be the same. Table 7 presents the simulation conditions. Fig. 19 shows and compares the resultant bed profiles in the four Runs and Table 8 presents the quantitative results of this simulation. They clearly show the deepening of the toe scour as the freeboard increases. Higher freeboard decreases the portion of the wave that overtops, which is indicated by smaller q value. This consequently generates the reflected wave with higher amplitude and thus increase the height of the resultant standing wave, which is indicated by higher H_m.

The steady streaming under the surface of the four Runs are presented in Fig. 20 and the spatial distribution of bottom velocities are presented in Fig. 21. In Run 3 (Fig. 20(a)), most of the fluid move towards the breakwater and the re-circulating cells are not too visible to form. Zero horizontal bottom velocity (U_{bm}) is observed close to the toe, at $x=5.75$ m, which is the area under the halfway of the 1st node and antinode of standing wave. It indicates that no fluid movement induces sediment movement in that area, which is the reason of why there is no toe scour in the bed profile of Run 3 in Fig. 19. The re-circulating cells begin to form as the freeboard increases, in which an anticlockwise re-circulating cell appears to form in front of the breakwater toe in Fig. 20(c). This cell becomes more visible in Fig. 20(d). These anticlockwise cells amplify the flow velocity at the bottom. In Fig. 21, it is shown that the fluids flow away from the breakwater, indicated by the negative values of U_{bm}, towards the 1st node of the standing wave ($x=5.5$ m) with greater velocity as the freeboard increases. This causes the deepening of toe scours in Runs. 1, 7, and 10 of Fig. 19.

5. Conclusions

The hydrodynamics and scour/deposition pattern offshore of impermeable vertical breakwaters under the effects of wave overtopping were investigated based on the numerical experiments. Special attention was given to the effects of overtopping with different discharges. Different wave conditions and breakwater heights (freeboards) were considered as the factors that change the overtopping discharge. The RANS-VOF model of Tofany et al. (2014) was used for the present simulations. It was found that the predicted fluid velocities were in good agreements with the experimental data and analytical solution. It has also been shown that the model showed better predictions of the scour/deposition patterns and maximum scour depths than the existing models. Based on the numerical results obtained, the following conclusions are made:

1. The results of the first numerical experiment show that overtopping reduces the energy of the incident wave. It then turns the profile of the resultant standing wave and the structure of steady streaming offshore of the breakwater, becoming more asymmetrical. Subsequently, the magnitude of velocity at the bottom is decreased, generating smaller scour depth/deposition height. The toe scour was even not formed offshore of the toe of the breakwater.
2. The changes of wave condition and freeboard have significant effects in changing the overtopping discharge. Different discharges then give sequential effects on the profile of the resultant standing wave on the surface, the pattern and magnitude of velocities in the steady streaming system under the surface, and finally on the resultant scour/deposition pattern at the bottom, especially the depth of the toe scour that can possibly affect the breakwater stability.
3. During the overtopping, the turbulence is generally generated instantaneously in the localized area on the crown of the breakwater. The generated turbulence is very small in magnitude and does not spread to the area offshore of the breakwater, thus it does not directly affect the structure of steady streaming and the generated scour/deposition pattern.
4. Higher incident wave and freeboard increase the height of the resultant standing wave; amplify the velocity at the bottom that subsequently induces more sediment movement at the bottom. Consequently, the depth of toe scour becomes deeper.

This study has shown the significance of the wave conditions and breakwater height (freeboard) in changing the overtopping discharge and thus the hydrodynamics and scour/deposition pattern offshore of the breakwater. In the light of these important findings, the present study may contribute to provide important suggestions for coastal engineers to carefully consider the wave condition and breakwater height in designing the breakwaters or other coastal structures. In the future, it is expected that the present numerical model can be used as a practical tool for predicting the hydrodynamics and the scour formation offshore of a breakwater. However, the long running time of the model has limited applicability of the model. For example, the model spent about 3 weeks to obtain a profile of the equilibrium scour/deposition pattern. Therefore, further developments will be focused on solving this problem. During this study, it was found that the iteration method used to solve the pressure field is most likely the main source of the running time problem. Improving the numerical solution for the pressure field and/or applying parallel computing seem potential to significantly reduce the running time.

Acknowledgments

The authors would like to thank the Minister of Higher Education, Malaysia (MoHE) for financially supporting this study through the research grants of Tabung Amanah MLNG-INOS (TE 67901).

References

Allsop, W., Bruce, T., Pearson, J., and Besley, P., 2005. Wave overtopping at vertical and steep seawalls. In: Proceedings of the ICE - Maritime Engineering, Vol. 158, pp. 103–114.

Bailard, J.A., 1981. An energetic total sediment transport model for a plane sloping beach. J. Geophys. Res. C11, 10938–10954.

Bakhtyar, R., Barry, D.A., Yeganeh-Bakhtiary, A., Ghaheri, A., 2009. Numerical simulation of surf swash zone motions and turbulent flow. Adv. Water Resour. 32, 250–263.

Bijker, E.W., 1971. Longshore transport computation. J. Waterw. Harbors Coast. Eng. Div. ASCE97 WW4, 687–701.

Changkuan, Z., 1994. Cross-Shore Sediment Transport: Analysis of Delta Flume Data and Mathematical Modelling (Communications on Hydraulics and Geotechnical Engineering). Faculty of Civil Engineering, Delft University of Technology.

de Best, A., Bijker, E.W., 1971. Scouring of a Sand Bed in Front of a Vertical Breakwater. Department of Civil Engineering, Delft University of Technology.

Engelund, F.A., Fredsøe, J., 1976. A sediment transport model for straight alluvial channels. Nord. Hydrol. 7 (5), 293–306.

Pullen, T., Allsop, N.W.H., Bruce, T., Kortenhaus, A., Schuttrumpf, H., van der Meer, J. W., 2007. Wave overtopping of sea defences and related structures: assessment manual. EurOtop Team.

Fredsøe, J., Deigaard, R., 1992. Mechanics of Coastal Sediment Transport. World Scientific, Singapore.

Gislason, K., Fredsøe, J., Sumer, B.M., 2009a. Flow under standing wave. Part 1: Shear stress distribution, energy flux and steady streaming. Coast. Eng. 56, 341–362.

Gislason, K., Fredsøe, J., Sumer, B.M., 2009b. Flow under standing wave. Part 2: Scour and deposition in front of breakwaters. Coast. Eng. 56, 363–370.

Hajivalie, F., Yeganeh-Bakhtiary, A., Houshanghi, H., Gotoh, H., 2012. Euler–Lagrange model for scour in front of vertical breakwater. Appl. Ocean Res. 34, 96–106.

Hirt, C.W., Nichols, B.D., 1981. Volumeof fluid (VOF) method for the dynamics of free surface boundaries. J. Comput. Phys. 39, 201–225.

Hughes, S.A., Fowler, J.E., 1991. Wave-induced scour prediction at vertical walls. In: Proceedings of the Conference Coastal Sediments. Vol. 91, pp. 1886–1899.

Irie, I., Nadaoka, K., 1984. Laboratory reproduction of seabed scour in front of breakwaters. In: Proceedings of the 19th International Conference on Coastal Engineering, Houston, TX. Vol. 2, 26, pp. 1715 – 1730.
Jonsson, I.G., 1966. Wave boundary layer and friction factors. In: Proceedings of the 10th Coastal Engineering Conference.
Karambas, T.V., 1998. 2DH non-linear dispersive wave modelling and sediment transport in the nearshore zone. In: Proceeding of the International Conference of Coastal Engineering (ICCE), pp. 2940–2953.
Lakhan, V.C., 2003. Advances in Coastal Modelling. Elsevier Science Publishing Company, The Netherlands.
Launder, B.E., Spalding, D.B., 1974. The numerical computation of turbulent flow. J. Comput. Mech. Appl. Mech. Eng. 3, 269–289.
Lee, K., Mizutani, N., 2008. Experimental study on scour occurring at a vertical impermeable submerged breakwater. Appl. Ocean Res. 30 (2), 92–99.
Leliavsky, S., 1955. An Introduction to Fluvial Hydraulics. Constable, London, p. 245.
Lillycrop, W.J., Hughes, W.J., 1993. Scour Hole Problems Experienced by the Corps Of Engineers; Data Presentation and Summary. US Army Engineer Waterway Experiment Station. Coastal Engineering Research Center, Vicksburg, MS.
Lin, P., Liu, P.L.F., 1998. A numerical study of breaking waves in the surf zone. J. Fluid Mech. 359, 239–264.
Miche, A., 1944. Mouvementsondulatoires de la mer en profondeurcroissanteoudécroissante. Première partie. Mouvementsondulatoirespériodiquesetcylindriques en profondeurconstante. Ann. Ponts Chaussèes 114, 42–78.
Müller, G., Allsop, NWH, Bruce, T., Kortnhaus, A., Pearce, A., and Sutherland, J., 2008. The occurrence and effects of wave impacts. In: Proceedings of the ICE- Maritime Engineering. Vol. 160 (4), No. 4, pp. 167–173.
Nichols, B.D., Hirt, C.W., Hotchkiss, R.S., 1980. SOLA-VOF: A Solution Algorithm for Transient Fluid Flow With Multiple Free Boundaries (Report LA–8355). Los Alamos Scientific Laboratory,University of California.
Oumeraci, H., 1994. Review and analysis of breakwater failures- lessons learned. Coast. Eng. Special Issue Vert. Breakwaters 22, 3–29.
Patankar, S.V., 1980. Numerical Heat Transfer and Fluid Flow. Hemisphere, NewYork.
Petit, H.A.H., vanGent, M.R.A., van den Boscj, P., 1994. Numerical Simulation and Validation of Plunging Breakers Using a 2D Navier–Stokes Model. ASCE, Kobe, Japan, pp. 511–524.
Reeve, D., Chadwick, A., Fleming, C., 2004. Coastal Engineering: Processes, Theory, and Design Practice. Spon Press, London and New York.
Soulsby, R.L., 1997. Dynamics of Marine Sands. Thomas Telford, London.
Sumer, B.M., Fredsøe, J., 2000. Experimental study of 2D scour and its protection at a rubble-mound breakwater. Coast. Eng. 40, 59–87.
Sumer, B.M., Whitehouse, R.J.S., Tørum, A., 2001. Scour around coastal structures: a summary of recent research. Coast. Eng. 44, 153–190.
Sumer, B.M., Fredsøe, J., Lamberti, A., Zanuttigh, B., Dixen, M., Gislason, K., Penta, A. F.D., 2005. Local scour at roundhead and along the trunk of low crested structures. Coast. Eng. 52 (10–11), 995–1025.
Tahersima, M., Yeganeh-Bakhtiary, A., Hajivalie, F., 2011. Scour pattern in front of vertical breakwater with overtopping. J. Coast. Res. SI 64, 598–602.
Tofany, N., Ahmad., M.F., Kartono, A., Mamat, M., Mohd-Lokman, H., 2014. Numerical modeling of the hydrodynamics of standing wave and scouring in front of impermeable breakwaters with different steepnesses. Ocean Eng. 88, 255–270.
Torrey, M.D., Cloutman, L.D., Mjolness, R.C., Hirt, C.W., 1985. NASA-VOF2D: A Computer Program for Incompressible Flows with Free Surfaces (Report LA–10612–MS). Los Alamos Scientific Laboratory, University of California.
Xie, S.L., 1981. Scouring Pattern in Front of Vertical Breakwaters and their Influence on the Stability of the Foundation of the Breakwaters (Report). Department of Civil Engineering, Delft University of Technology, Delft, Netherlands..
Yeganeh-Bakhtiary, A., Hajivalie, F., Hashemi-Javan, A., 2010. Steady streaming and flow turbulence in front of vertical breakwater with overtopping. Appl. Ocean Res. 32, 91–102.
Young, D.M., Testik, F.Y., 2011. Wave reflection by submerged vertical and semicircular breakwaters. Ocean Eng. 38, 1269–1276.
Zhang, S., Cornett, A., Li, Y., 2001. Experimental study of kinematic and dynamical characteristics of standing wave. In: Proceedings of the 29th International Association of Hydro-Environment Engineering and Research Conference.